NANO · MICRO small
www.small-journal.com

A Nanoparticle Ink Allowing the High Precision Visualization of Tissue Engineered Scaffolds by MRI

*Samila Leon-Chaviano, Mariia Kiseleva, Philippe Legros, Simon Collin, Théophraste Lescot, Céline Henoumont, Yves Gossuin, Sophie Laurent, Dominique Mayrand, Julie Fradette, André Bégin-Drolet, Jean Ruel, and Marc-André Fortin**

Hydrogels are widely used as cell scaffolds in several biomedical applications. Once implanted in vivo, cell scaffolds must often be visualized, and monitored overtime. However, cell scaffolds appear poorly contrasted in most biomedical imaging modalities such as magnetic resonance imaging (MRI). MRI is the imaging technique of choice for high-resolution visualization of low-density, water-rich tissues. Attempts to enhance hydrogel contrast in MRI are performed with "negative" contrast agents that produce several image artifacts impeding the delineation of the implant's contours. In this study, a magnetic ink based on ultra-small iron oxide nanoparticles (USPIONs; <5 nm diameter cores) is developed and integrated into biocompatible alginate hydrogel used in cell scaffolding applications. Relaxometric properties of the magnetic hydrogel are measured, as well as biocompatibility and MR-visibility (T_1-weighted mode; in vitro and in vivo). A 2-week MR follow-up study is performed in the mouse model, demonstrating no image artifacts, and the retention of "positive" contrast overtime, which allows very precise delineation of tissue grafts with MRI. Finally, a 3D-contouring procedure developed to facilitate graft delineation and geometrical conformity assessment is applied on an inverted template alginate pore network. This proof-of-concept establishes the possibility to reveal precisely engineered hydrogel structures using this USPIONs ink high-visibility approach.

1. Introduction

Hydrogels are water-rich, tridimensional (3D) polymer networks that can be found in an increasing number of biomedical applications such as regenerative medicine,[1] diabetes therapy,[2] drug delivery,[3] and topical administration of drugs on skin and mucosa.[4] In particular, regenerative medicine is an area of research aiming at developing functional tissues potentially implantable in vivo. Applications are numerous: fat tissue grafts, myocardium regeneration, bone healing, etc. Once introduced in vivo, these new tissues must integrate into the body, and this verification step often requires biomedical imaging follow-up. Unfortunately, engineered tissues are often made of cells that are distributed in 3D polymer networks that neither show intrinsic contrast in X-ray computed tomography (CT) nor in magnetic resonance imaging (MRI). The latter modality is of particular interest for the imaging of soft tissues, in which

S. Leon-Chaviano, M. Kiseleva, P. Legros, T. Lescot, D. Mayrand, J. Fradette, M.-A. Fortin
Centre de Recherche du Centre Hospitalier Universitaire de Québec – Université Laval (CR CHUQ)
Axe Médecine Régénératrice
Quebec City, Québec G1L 3L5, Canada
E-mail: marc-andre.fortin@gmn.ulaval.ca

S. Leon-Chaviano, M. Kiseleva, P. Legros, T. Lescot, M.-A. Fortin
Département de Génie des Mines de la Métallurgie et des Matériaux
Université Laval
Quebec City, Québec G1V 0A6, Canada

The ORCID identification number(s) for the author(s) of this article can be found under https://doi.org/10.1002/smll.202206644.

DOI: 10.1002/smll.202206644

S. Collin, A. Bégin-Drolet, J. Ruel
Département de Génie Mécanique
Université Laval
Quebec City, Québec G1V 0A6, Canada

C. Henoumont, S. Laurent
Département de Chimie Générale
Organique et Biomédicale
Université de Mons
Mons 7000, Belgium

Y. Gossuin
Service de Physique Biomédicale
Université de Mons
Mons 7000, Belgium

D. Mayrand, J. Fradette
Département de Chirurgie
Faculté de Médecine
Université Laval
Quebec City, Québec G1V 0A6, Canada

J. Fradette
Centre de Recherche en Organogénèse Expérimentale de l'Université Laval/LOEX
1401, 18e rue, Quebec City, Québec G1J 1Z4, Canada

density variations are very subtle and thus not easily differentiated by CT scanning.

Cell-loaded hydrogels are now used in tissue regeneration, post-surgical procedures, and wound healing applications.[1a,5] Hydrogels can reproduce certain physical, chemical, electrical, and biological properties of natural tissues' matrices.[6] These properties make them adaptable for either temporary or long-term cell scaffolds.[7] Cell-containing biomedical hydrogel scaffolds must be designed following these criteria: 1) minimal cytotoxicity, which includes the polymer, its crosslinking reagents, and side products; 2) uniformity of the structural and geometrical design of the scaffolds; 3) adequate porosity, which is crucial for bringing the nutrients and oxygen to cells and also to evacuate metabolic wastes efficiently.[7a,8] Therefore, hydrogels must be carefully chosen with respect to their biocompatibility, viscosity, and crosslinking strategies. Natural hydrogels (e.g., alginate, chitosan, gelatin) can be adapted to provide a biocompatible environment to cells.[9] More importantly, most natural hydrogels require mild conditions for crosslinking, therefore, limiting the generation of potentially harmful side products (e.g., radical initiators). Alginate, in particular, is increasingly used in tissue engineering and procedures involving molded and 3D-printed hydrogels.[8,10] This polymer crosslinks in contact with bivalent ions, such as calcium, contained in the living tissues.[9a,11] It is a polysaccharide made of alternating β-D-mannuronate (M) and α-L-guluronate (G) units; the latter is involved in the crosslinking process.[12]

When used as cell scaffolds, hydrogels are formed into objects of various levels of complexity depending on the tissue or the part of the organ they aim at replacing. Within these volumes, the design of interconnected channels to facilitate nutrients and oxygen transport, as well as vascular growth, is a promising approach. To visualize and assess the geometry of such complex shapes and pore structures before and after their insertion in the body, biomedical imaging is required. Among the various imaging techniques available to visualize hydrogel biomaterials, including cell-containing scaffolds, fluorescence imaging is probably the most commonly used in vitro.[13] However, once integrated into biological host tissues after grafting, the fluorophores cannot be efficiently triggered and detected, due to the strong diffusion of visible photons at the millimeter level depth. CT on the other hand generates too poor contrast between tissues of similar density. Moreover, repeated exposure to X-rays is toxic to cells, and this would probably rule out the use of CT for clinical follow-up assessments.[14] Finally, positron emission tomography (PET) is a metabolic technique that requires radiotracers, and it is not adapted for geometrical assessments because it is limited in resolution.

MRI is an imaging modality widely used both in pre-clinical and clinical studies. It is perhaps the best technique to visualize soft tissues at anatomical resolution. In MRI, the signal comes from the precession of low-energy nuclear spins, usually, hydrogen protons, excited by a radiofrequency pulse tuned to match their Larmor frequency at a specific magnetic field strength.[15] After initial excitation, the spins return to equilibrium through longitudinal and transverse relaxation, respectively, characterized by the longitudinal (T_1) and transverse (T_2) relaxation times, which are specific to each biological tissue visualized in MRI. In fact, T_1 and T_2 parameters are used to generate contrast in MRI, and contrast agents developed for this modality have a preferential effect either on one, on the other, or both parameters. Without the use of an adequately selected contrast agent, hydrogels implanted in vivo would be difficult to differentiate from many soft tissues located in their surroundings.

Contrast agents in MRI are mainly of two kinds: the ones that give rise to a darkening effect (T_2/T_2*-weighted; "negative" contrast agents) and the ones that give rise to an increase of signal (T_1-weighted; "positive" contrast agents). For hydrogel visualization, positive contrast enhancement through a shortening effect on the longitudinal relaxation time is preferred because it is largely free of the magnetic susceptibility-related artifacts caused by T_2* effects. Until now, only a few attempts have been reported on positively-contrasted hydrogels by employing gadolinium-based products.[13b,16] However, the known toxicity of Gd^{3+} and its potential release and bioaccumulation could lead to serious health issues including nephrogenic systemic fibrosis.[17] A few studies have reported on the use of superparamagnetic iron oxide nanoparticles (SPIONs; less than 20 nm in core size) which produce a negative contrast in T_2-weighted imaging.[18] Several SPIONs formulations have been approved by health authorities for different diagnostic and therapeutic applications over the past 20 years (e.g., ferumoxytol),[19] while other formulations of SPIONs are currently under clinical trials for hyperthermia treatments or as MRI contrast agents.[20] However, the "negative" contrast usually produced by SPIONs can impede the generation of large "clouds" devoid of signal, that extend far beyond the areas where the hydrogel is located.[21]

In the last decade, significant progress was made in the synthesis of very small iron oxide nanoparticles of uniform size.[22] Also called extremely or ultra-small SPIONs (USPIONs), these particles feature a moderate magnetization (i.e., limited T_2 shortening contribution) and a strong impact on the longitudinal relaxivity (T_1). In T_1-weighted imaging, they generate a "positive" contrast effect.[23] Hydrophilic ligands, such as poly(ethylene glycol) (PEG), have been successfully employed to promote longitudinal relaxivity, biocompatibility, and colloidal stability in water.[24]

In this study, an MRI-visible alginate-based hydrogel formulation containing USPIONs was developed, thereby allowing geometrical quality assessments of complex-shaped hydrogel scaffolds. Oleic acid-stabilized USPIONs having a core size of 5 nm were synthesized using a thermal decomposition technique followed by a highly effective ligand substitution method using PEG-derivative ligands (**Figure 1**a). PEG-stabilized USPIONs with low polydispersity were fully characterized (size, surface ligands, magnetic properties) and showed very strong T_1-weighted contrast properties, close to that achieved by gadolinium-based contrast agents. USPIONs were then incorporated into alginate hydrogels, and a complete relaxometric and magnetic characterization procedure was performed to clearly demonstrate that USPIONs, once adequately and uniformly dispersed in hydrogels, retain their positive contrast properties. The visibility of the alginate-USPION hydrogels was demonstrated in vivo (mouse model), and grafts were followed-up for a period of 2 weeks. The biocompatibility of the implants was studied by measuring inflammatory markers in

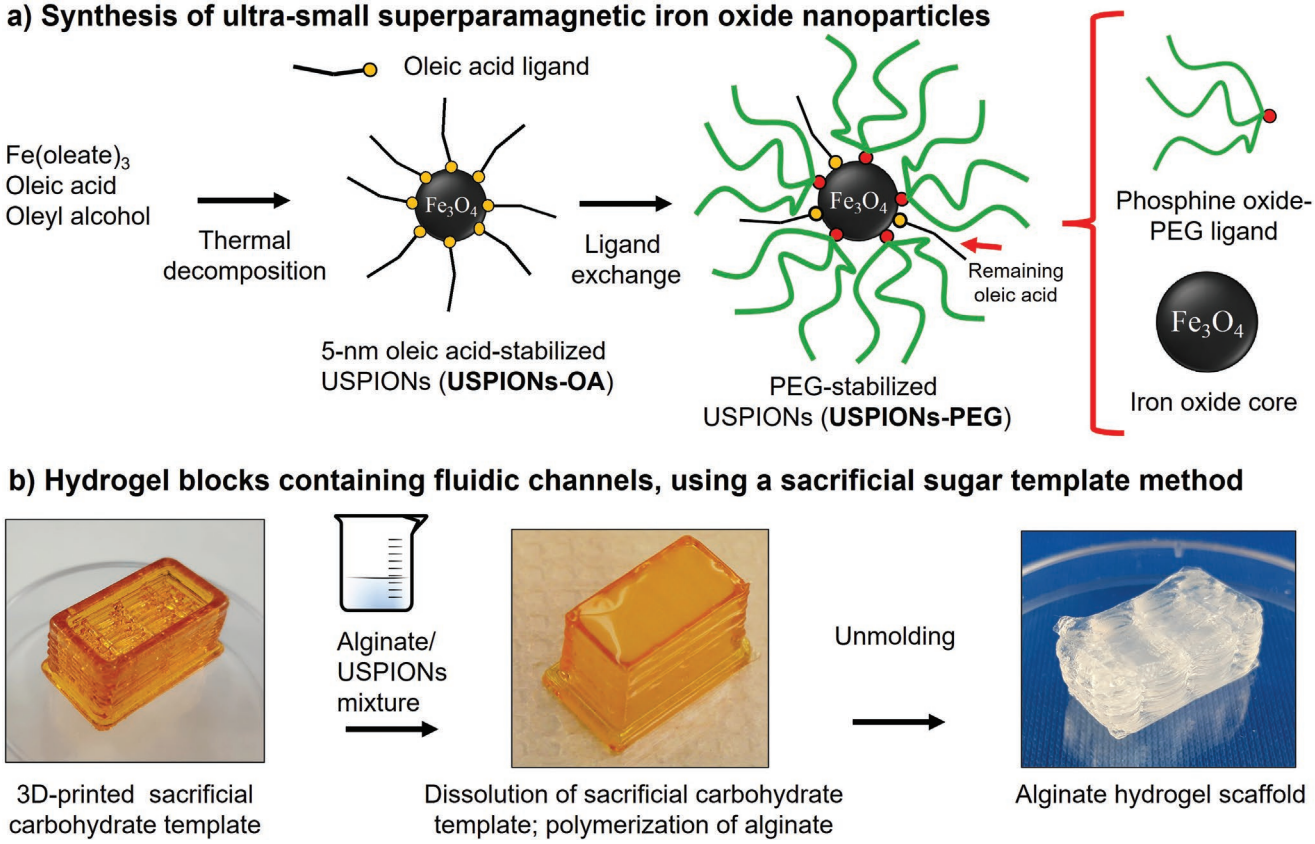

Figure 1. Schematic representation of a) USPIONs synthesis and b) preparation of contrast-enhanced hydrogels containing fluidic channels, using an inverted template casting technique. The iron oxide nanoparticles are incorporated into the hydrogel mixture, which is casted onto a 3D-structured carbohydrate sacrificial template. Upon dissolution of this carbohydrate-based template, a hydrogel object containing fluidic channels is produced, made of crosslinked alginate hydrogel and USPIONs (b, right).

the blood (in vivo experiments), as well as by demonstrating that adipose-derived stem/stromal cells (ASCs) exposed to the hydrogels retain their differentiation potential into adipocytes (in vitro experiments). Finally, the precision achieved in the measurement by MRI of complex, sub-millimetric forms in USPION-supplemented alginate structures, was demonstrated by using hydrogel volumes riddled with oriented pores generated by an original sugar printing technology approach producing inverted template pore networks in alginate objects (Figure 1b). Overall, this proofs-of-concept establish well the potential of USPIONs as an additive for cell scaffold volume and shape follow-up procedures in vivo.

2. Results and Discussion

2.1. Synthesis and Characterization of Nanoparticle Ink Made of USPIONs

PEGylated USPIONs were prepared by the thermal decomposition technique followed by ligand exchange using PEG-derivatized phosphine oxide (PO-PEG). PO-PEG ligands were prepared by mixing methyl-PEG (mPEG) in presence of $POCl_3$, which is highly reactive to the alcohol moieties of the methyl-PEG precursor. The resulting PO-PEG was characterized using ^{31}P nuclear magnetic resonance (NMR,Figure S1, Supporting Information). **Figure 2**a,b shows the size comparison of USPIONs before and after ligand exchange. Very high iron concentrations were achieved by this technique compared with more conventional PEGylation procedures: 45 ± 3 mM Fe, down from 123 ± 3 mM Fe for the oleic acid-stabilized USPIONs before ligand exchange. Successful ligand exchange was confirmed by the visual inspection of a two-phase hexane-water suspension showing the iron oxide nanoparticles (red-orange color) dispersed first in hexane, and then in water (Figure 2c, inset).

The mean size of USPIONs-PEG (4.9 ± 0.9 nm) reflects their potential as "positive" contrast agents in T_1-weighted MRI (i.e., <5 nm).[23,25] The low polydispersity distributions (≈17% error) indicate that the ligand exchange procedure did not affect the average size of the colloids. Hydrodynamic diameters measured by dynamic light scattering (DLS) were 8.9 ± 0.2 and 20 ± 0.6 nm for USPIONs-OA and USPIONs-PEG, respectively (intensity-weighted profiles in Figure 2c). The increase in hydrodynamic size after ligand substitution was attributed to the bulkiness of the PO-PEG, which has three linear PEG chains. The colloids were stable for 30 days in NaCl, phosphate-buffered saline (PBS), and complete Dulbecco's Modified Eagle's Medium (DMEM) solution (Figure S2, Supporting Information).

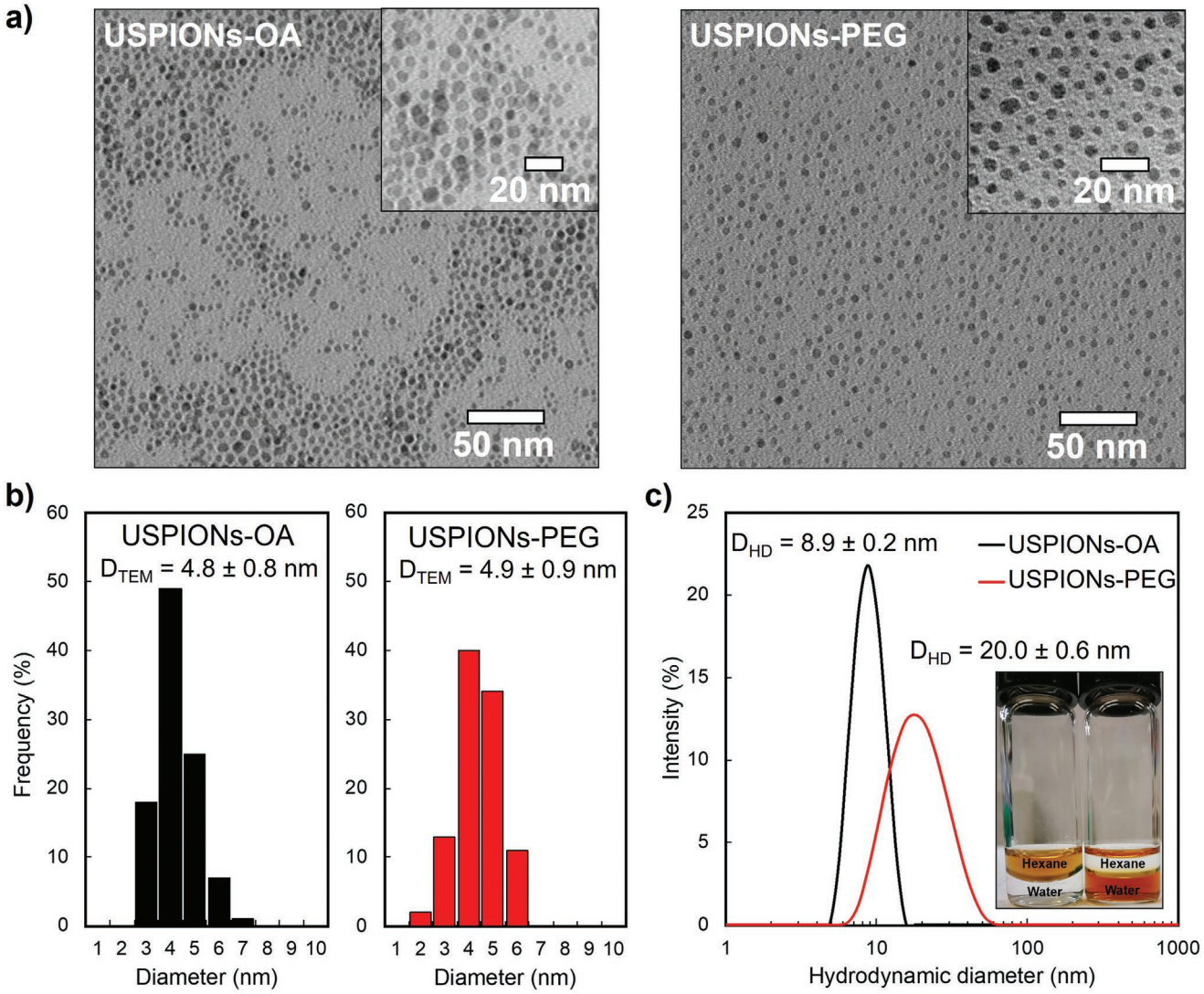

Figure 2. Particle size analysis of oleic acid-stabilized USPIONs (USPIONs-OA) in hexane, and PEG-stabilized USPIONs (USPIONs-PEG) in water. a) Representative TEM images before and after ligand exchange. b) TEM size distribution profile ($n = 100$). c) Intensity-weighted hydrodynamic diameter profiles (inset: photography showing USPIONs-OA dispersed in hexane and USPIONs-PEG dispersed in water). Results are shown as mean ± SD. DHD: hydrodynamic diameter.

Fourier transform infrared (FTIR) spectroscopy measurements were performed to reveal ligand grafting at the particle's surface, whereas TGA analysis was performed to measure the density of PEG grafting (see Figures S3 and S4, Supporting Information). In all FTIR spectra, the typical Fe—O vibration was observed for both samples, confirming the presence of iron oxide cores (Figure S3, Supporting Information). For USPIONs-OA, the spectrum showed C—H and C=O stretching bands that are characteristic of oleic acid; on USPIONs-PEG, ligand exchange was confirmed by the presence of intense C—O—C vibration bands from the PEG molecules (Figure S3, Supporting Information). With TGA (Figure S4, Supporting Information), the number of ligands was estimated to be 147.8/USPION for USPIONs-OA and 46.1/USPION for USPIONs-PEG (PEG is a bulky ligand). The magnetization curves were measured for both colloids, and they revealed a behavior indicating superparamagnetism. Saturation magnetizations of 62 and 56 $Am^2\ kg^{-1}$(Fe) for USPIONs-OA and USPIONs-PEG, respectively (Figure S5, Supporting Information), are in agreement with values reported in the literature for USPIONs of similar size (≈5 nm Fe_3O_4 nanoparticles).[22a,25] Finally, as a complement, scanning electron microscopy (SEM) images of lyophilized hydrogels can be found in the Supporting Information section (Figure S6, Supporting Information).

2.2. Relaxometric Properties and NMRD Profiles

The relaxation rates (i.e., $1/T_1$; $1/T_2$) of aqueous suspensions containing USPIONs-PEG were measured at clinically-relevant magnetic field strength (1.41 T) (**Figure 3**a). USPIONs-PEG colloids showed a longitudinal (r_1) and a transverse (r_2) relaxivity of 7.5 and 22.9 $mM^{-1}s^{-1}$, respectively, for an r_2/r_1 ratio of 3.05. This value falls in the category of "positive" contrast agents. These

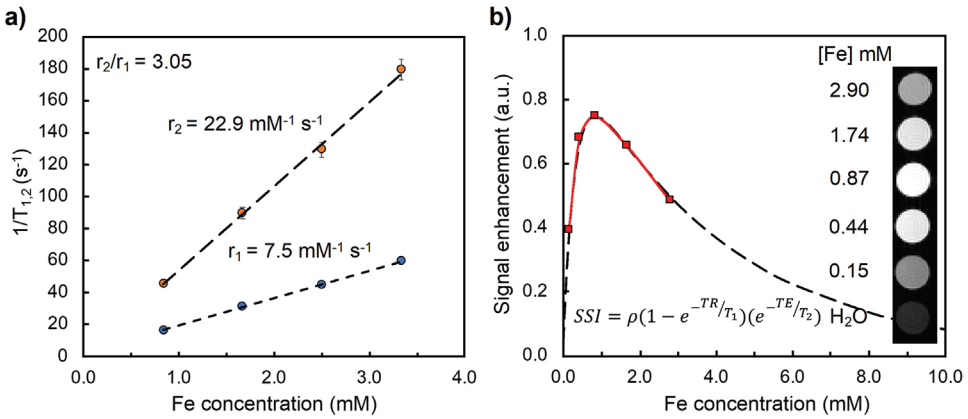

Figure 3. a) Relaxation rates ($1/T_1$; $1/T_2$) of USPIONs-PEG in water (25 °C, 1.41 T). Results are shown as mean ± SD. b) Simulated MRI signal (dotted black line; using Equation (2) in the Experimental Section; TR = 400 ms, TE = 10.8 ms) and signal measured experimentally by MRI (full red line) at 25 °C and in a 1 T field. Inset: T_1-w. MRI results for the corresponding colloids.

results were found similar to the relaxivities of other ultra-small (<7 nm) iron oxide colloids published in the literature: multidentate block copolymer-stabilized USPIONs (r_2/r_1 = 3.8–5),[22a,e,26] PEGylated USPIONs (r_2/r_1 = 3.4),[27] PO-PEG-stabilized USPIONs (r_2/r_1 = 1.4–3.6, 3 T), as well as Supravist (SHU-555C; hydrodynamic size of 21 nm; transmission electron microscope (TEM) size of 3–5 nm; longitudinal relaxivity of 10.7 mM^{-1}s^{-1} and r_2/r_1 of 3.55 at 1.5 T (37 °C)).[20,22b,28] In T_1-w. MRI, an optimal signal was found for this colloid system at a concentration of 0.87 mM Fe at 1 T (Figure 3b).

A stability assay was performed by assessing the relaxation times for up to 30 days in NaCl, PBS, and complete DMEM solution (DMEM + 10% fetal bovine serum [FBS] + 1% penicillin), and by comparing these values with colloidal stability results performed by DLS measurements (Figure S7, Supporting Information). For USPIONs in complete DMEM, a slight shift of the main peak toward higher hydrodynamic diameters occurred after 30 days, which was assumed to be related to protein corona thickening, as well as to the possibility of slight agglomeration. All the other results (hydrodynamic diameter, T_1 and T_2) were perfectly stable over a period of 30 days.

The relaxometric analysis was further refined by measuring nuclear magnetic relaxation dispersion (NMRD) profiles on both USPIONs colloids and with USPIONs in hydrogels (**Figure 4**). These profiles were acquired to study the evolution of the longitudinal and transverse relaxivities (r_1, r_2) of USPIONs-PEG in aqueous solution and alginate (hydrogel) at various concentrations (1–5 wt%) in the range of 0.1–500 MHz (2 mT to 11.7 T, Figure 4). For a matter of simplicity, only the NMRD profile of 2 wt% alginate-based hydrogel is shown in Figure 4, however, all NMRD profiles can be found in the Supporting Information (Figure S8, Supporting Information). The experimental data curves were fitted, which allowed extracting an estimated value for the crystal size and magnetization according to the Roch et al. model.[29] Longitudinal relaxivities for the 2 wt% alginate formulation, compared in Figure 4a, reveal a similar relaxometric behavior in both environments (water vs alginate hydrogel), with a slight decrease of the values when USPIONs are within the hydrogel. In the low field region (0.1–1 MHz), the longitudinal relaxivity was 9.57 and 7.54 mM^{-1} s^{-1} for USPIONs-PEG and hydrogel+USPIONs-PEG, respectively. The r_1 at the low field is governed by the anisotropy energy of the iron oxide crystal. The small decrease noted for r_1 values at 1 MHz for both USPIONs-PEG hydrogel+USPIONs-PEG, indicates low anisotropy energy. Then, at moderate-to-high magnetic field strengths, Curie relaxation occurs leading to a peak (Curie peak), which is then followed by a radical r_1 decrease at >30 MHz. This is a typical characteristic of colloidal suspensions of SPIONs. From the fittings and according to the Roch et al. model, the peaks were found to be approximately centered at 20 MHz, thus the mean crystal size was estimated to be 7.6 and 6.6 nm for USPIONs-PEG in water and alginate hydrogel, respectively. This is quite consistent with the crystal core measurements with TEM reported in Figure 2 (4.8 ± 0.8 nm). Magnetizations of 38 and 40 Am^2 kg^{-1} were found for USPIONs-PEG and hydrogel+USPIONs-PEG, respectively, and these are also in agreement with the magnetization curve (Figure S5, Supporting Information).

Figure 4b reveals the evolution of r_1 and r_2 values along the magnetic field strength (USPIONs-PEG vs USPIONs-PEG crosslinked with 2 wt% alginate). Both samples follow the same trend: the r_1 curves are relatively constant at low magnetic field strengths, then decrease at 30 MHz, whereas the r_2 curves increase rapidly and then saturate at high field strengths. This observation follows the Langevin function according to which at increasing magnetic field strengths, nanoparticle magnetization increases up to saturation.[23] By comparing the longitudinal and the transverse relaxivity values (Figure 4b), is it clear that the entrapment of USPIONs into the hydrogel network has a higher incidence on the transverse relaxivity values, thus indicating the necessity to keep the iron concentration at low values as possible in order to avoid the signal quenching effect in particular at higher magnetic field strengths (according to Equation (2)).

Figure 4c compares the r_2/r_1 values of colloidal USPIONs with that of USPIONs in different concentrations of hydrogel and at various magnetic field strengths (20, 60, 300, and 500 MHz; see Table S1, Supporting Information, for a complete list of r_1, r_2, and r_2/r_1 values). At high magnetic field strengths,

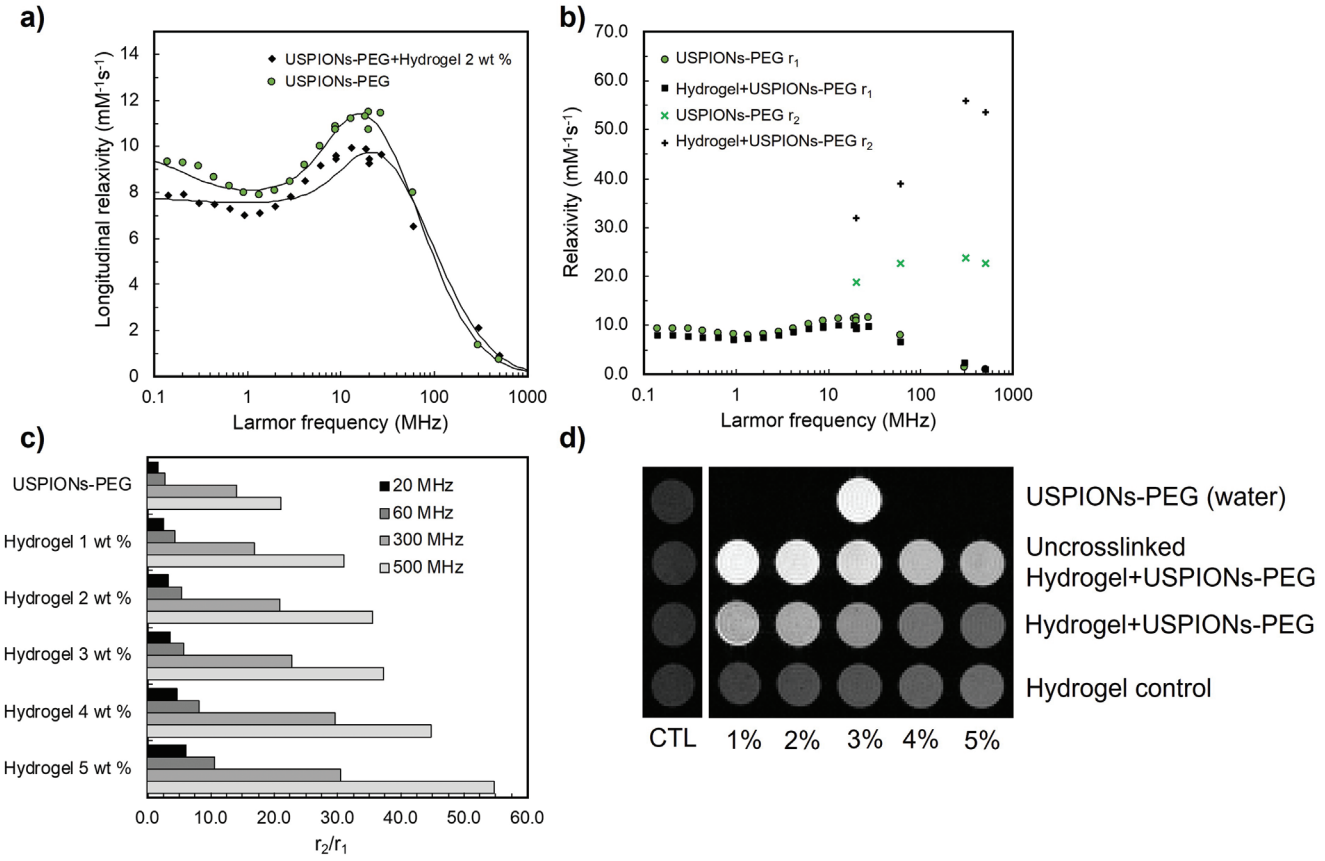

Figure 4. a) NMRD profiles (longitudinal relaxivity). b) r_1 and r_2 profiles of USPIONs-PEG in aqueous suspension (green dots), and USPIONs-PEG in a 2 wt% crosslinked alginate hydrogel (black dots) from 0.1 to 500 MHz at 25 °C (1 mM Fe). c) r_2/r_1 ratio values of USPIONs-PEG (1 mM Fe) in aqueous suspension and various crosslinked alginate hydrogel concentrations at 20, 40, 300, and 500 MHz (25 °C). d) T_1-weighted MRI (46.2 MHz, 1 T, 25 °C; TR = 400 ms; TE = 10.8 ms; CTL = water) of a 96-wells plate of USPIONs-PEG in aqueous suspension, uncrosslinked hydrogel+USPIONs-PEG, hydrogel+USPIONs-PEG (0.87 mM Fe), with hydrogel controls.

the r_2 values increase much more significantly for hydrogels. This evidence represents a possible limitation in the use of USPIONs-supplemented hydrogels at magnetic fields higher than 100 MHz. At clinical magnetic field strength (1–3 T), however, and with hydrogel concentrations of 0–2%, the changes in r_2/r_1 ratios are very limited and thus allow to put the hydrogel in positive contrast in T_1-weighted MRI. For hydrogels at 2 wt%, an r_2/r_1 relaxometric ratio of 22.9/7.5 = 3.05 was observed (at 1 T), which is very similar to that observed for colloidal USPIONs in water. In Figure S7, Supporting Information, no drastic change in T_1/T_2 was observed (30 ms/11 ms = 2.72) in more than 30 days; for USPIONs in PBS, a slight change was observed at t = 6 h, with an increase in the T_1/T_2 ratio from 2.7 up to 2.9. Overall, these results do not indicate the presence of Fe(III) ions in the water, and further confirm the stability of these USPIONs in water, saline, PBS, and complete DMEM after a period of at least 30 days.

Figure 4d shows the impact of alginate concentration on the positive contrast obtained in T_1-w. MRI at 1 T, by using the optimal Fe concentration revealed in Figure 3b. The second and third rows of the hydrogel samples indicate a slight impact of alginate concentration on the signal, for both uncrosslinked (second row) and crosslinked (third row) hydrogels. Crosslinking might limit the amount of water molecules near the iron oxide particles, thereby impacting the longitudinal relaxivity of the hydrogels, which is clearly visible when comparing the signal intensity between uncrosslinked and crosslinked hydrogels for each concentration. Due to the absence in the scientific literature of articles reporting relaxivity measurements on alginate-coated ultra-small iron oxide nanoparticles, we believe this topic could be interesting for future study in this specialized field. The presence of Ca^{2+} ions as the crosslinking agent possibly also slightly affects the relaxometric properties and thus has a slight impact on positive contrast. Optimal MRI contrast was found at alginate concentrations below 3 wt%; therefore, 2 wt% was selected as an optimum for the biocompatibility experiments of the study. Overall, the NMRD profiles measured in this study confirmed the relatively modest impact of alginate hydrogel environments on the relaxivity of USPIONs colloids. The quality of USPIONs dispersion in the hydrogels though, is an important factor in maintaining their relaxometric performance, since agglomeration would lead to a drastic increase of r_2, thus resulting in a strong decrease in MRI signal. At higher alginate concentrations, denser hydrogel environments around the nanoparticles could restrict the diffusion of water close to iron oxide cores, with an impact on the relaxivity of the magnetic system (Figure S8, Supporting Information).

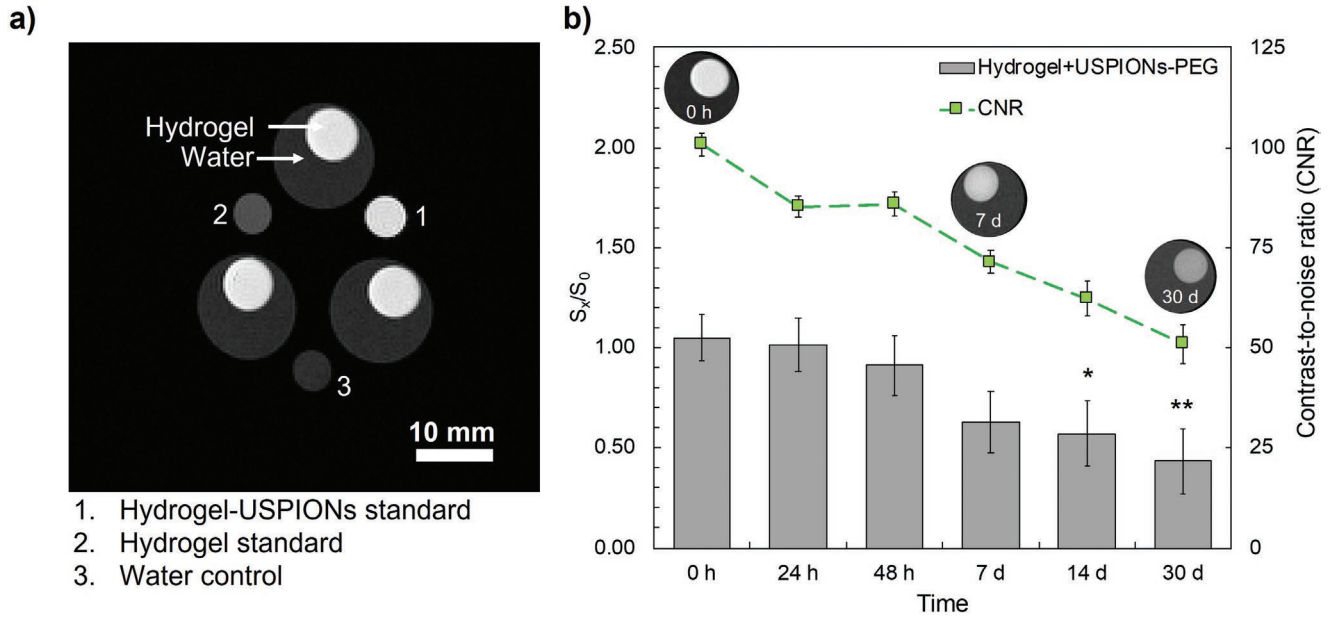

Figure 5. a) T_1-weighted MRI image (TR = 400 ms; TE = 10.8 ms) of three alginate hydrogel samples surrounded by water (in vitro experiments with controls). b) Signal stability and contrast-to-noise ratios of USPIONs-PEG-alginate hydrogels after a period of 30 days (incubation at room temperature). Evolution of signal (S_x/S_0 – left axis; gray column) and of contrast-to-noise ratio (CNR; right axis; green squares) for 2 wt% USPIONs-PEG-alginate hydrogels. S_x/S_0 comparison with 0 h was $*p < 0.05$ for comparison with 14 days, and $**p < 0.01$ for comparison with 30 days (n = 3). The results are represented as mean ± SD (n = 3). Insets: MRI images of hydrogels at 0 h, 7, and 30 days. After 30 days, a ≈2.5-fold CNR enhancement was still observed, which confirmed the possibility of a lasting contrast enhancement of the hydrogels over time.

2.3. Signal Stability of Hydrogels and Contrast-to-Noise Ratio Measurements

Hydrogel samples prepared at 0.87 mM Fe (optimal signal enhancement, as from Figure 3b) were immersed in water, visualized in MRI, and compared with controls (nanopure water, hydrogel, and hydrogel+USPIONs). The signal and the contrast effects were found stable for at least 48 h before a signal decrease was observed (**Figure 5**). The contrast-to-noise ratio (CNR) was measured at t = 0 (CNR = 102) and revealed an approximately fivefold CNR increase with respect to hydrogel without contrast agent ($CNR_{Hydrogel}$ = 19). The CNR was still very high after 7 and 14 days (≈3.5-fold CNR enhancement). After 7 days, the hydrogel+USPIONs-PEG retained about 50% of its initial brightness, indicating a slight release of the iron contents from the alginate. In Figure 5, the signal decrease in the hydrogels observed at t = 48 h most probably reflects the slight leakage of USPIONs from the porous hydrogel network, which is also suggested by the slight increase of signal in the supernatant (Figure S9, Supporting Information). Overall, this leakage does not affect the functionality of the hydrogels and the contours of the objects were still clearly delineated.

2.4. In Vitro Biocompatibility Assays with Hydrogel Products and Using Adipose Derived Stem/Stromal Cells

In the field of regenerative medicine, the surgical implantation of adipose tissues (mainly breast and facial tissues), could soon figure among the most MRI-intensive medical follow-up procedures. In this context, USPIONs inks integrated into cell culture scaffolds would greatly facilitate the delineation and follow-up of adipose tissue graft volumes. In the last two decades, the tolerance of different types of cells to USPIONs has been widely documented.[30] However, very little evidence of the ability of stem cells to retain their differentiation potential after incubation or contact with USPIONs has been reported.[31] For this reason, in this study, we specifically selected these cells to demonstrate the differentiation potential of ASCs into adipocytes. Indeed, among the various strategies aiming at engineering adipose grafts for reconstructive surgery, the use of precursor cells, such as ASCs, that are induced to differentiate into lipid-filled adipocytes is common.[32]

A schematic of the in vitro culture experiments is provided in Figure S9a, Supporting Information. First, the viability of ASCs after incubation with USPIONs-PEG (1 mM), D-(+)-gluconic acid δ-lactone (GDL) (0.5 mM), and alginate (1, 2, and 3 wt%), all products and concentrations relevant for the MRI procedures, was measured with the resazurin assay (Section S5, and Figure S10b, Supporting Information). At the concentrations used, neither USPIONs-PEG nor GDL or lower concentrations of alginate affect cell viability. However, the addition of 3 wt% alginate decreased cell viability down to 61%. These results oriented the decision to keep the alginate concentration at 2 wt% in the following in vivo experiments. The data are correlated by the appearance of the cultures at the cellular level (Figure S9c, Supporting Information).

Then, ASCs which were first exposed to the same hydrogel formulation products for 24 h, were subsequently differentiated into adipocytes using a classical adipogenic cell culture cocktail. The results (**Figure 6**) were compared with a set of diluent controls consisting of media and PBS (i.e., with the adipogenic

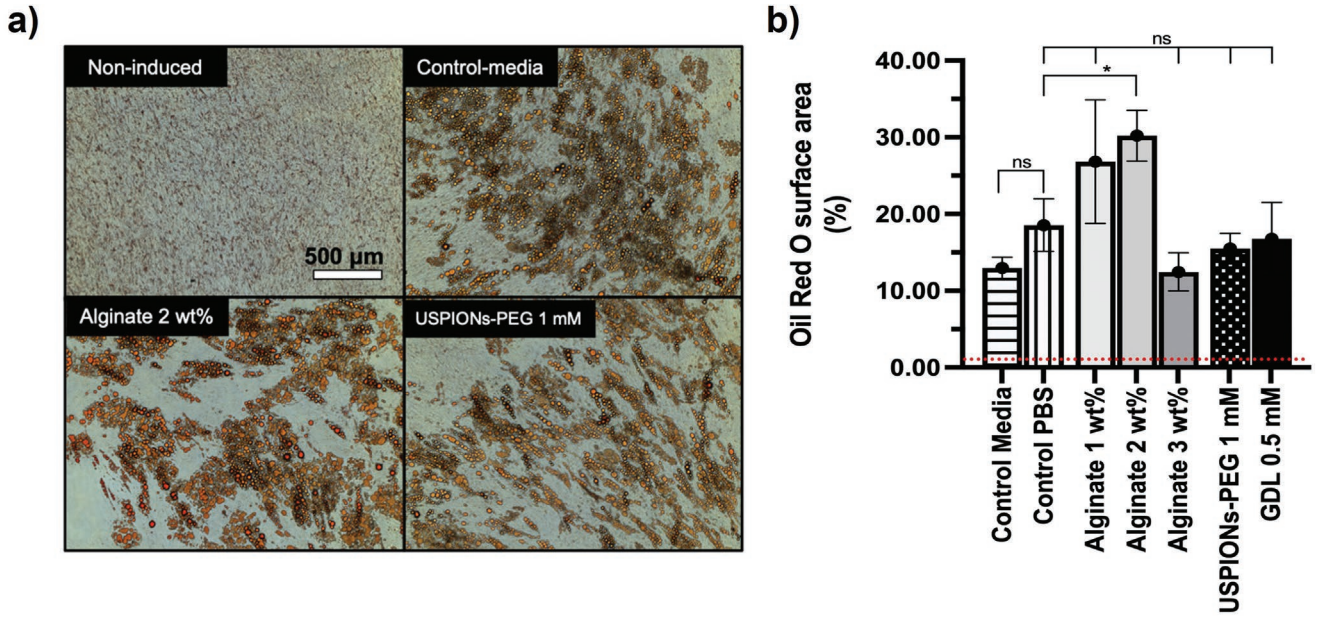

Figure 6. Differentiation of ASCs into adipocytes after 24 h exposure to alginate, USPIONs, and GDL. After 17 days of differentiation, the lipid content of cells was stained using Oil Red O, thus confirming the presence of adipocytes. a) Microscopy images of non-induced ASCs cells (i.e., without the use of an adipogenic cocktail), control-induced ASCs (exposed to cocktail in media only), ASCs exposed to alginate 2 wt%, and ASCs exposed to USPIONs-PEG at 1 mM (scale bar = 500 µm). b) Percentage of lipid area coverage evaluated from microscopy images, indicating the successful conversion of ASCs into adipocytes. The dotted line indicates background values for non-induced cultures. A one-way ANOVA analysis was applied with post-tests in comparison to the control-PBS group (* $p = 0.0194$).

cocktail but not exposed to the formulation products), as well as with uninduced cells (i.e., without the addition of the adipogenic cocktail, red dotted line). In a typical procedure, confluent cells (≈day 7) were differentiated and maintained in culture for 17 more days. At that time, the cells were treated with Oil red O (ORO) for staining the lipids, which allowed the measurement of the total surface area of the cultures covered by the adipocytes. The differentiation of these ASCs into adipocytes was thus highlighted by the presence of lipid-filled cells (Figure 6a and Figures S11 and S12, Supporting Information). Overall, these results confirm that alginate (1, 2, and 3 wt%), UPSIONs-PEG (1 mM), and GDL (0.5 mM) do not significantly affect the ability of ASCs to differentiate into adipocytes (Figure 6b). Even so, for the 2 wt% alginate group, a slight increase in lipid accumulation was measured, thus suggesting that the MRI-visible hydrogel formulation could be used to host ASCs without impeding their differentiation capability. On the microscopy images, the area covered by the adipocytes is similar to that of the controls (all below ≈20%). Interestingly, the exposure of ASCs to lower alginate concentrations (1–2 wt%) for 24 h seems to increase the lipid content to ≈27–30%.

2.5. In Vivo Biocompatibility Study of the Alginate-USPION Formulation

The USPION-alginate hydrogel formulation was injected in healthy BALB/c mice, and the volumes were monitored by MRI. Before injection, the alginate solutions were pre-crosslinked using $CaCO_3$ and GDL. After the addition of GDL, gelation occurred in about 3 min, which provided enough time to fill a syringe and perform the injection. Then, a spherical or elliptical bulge was clearly seen under the skin, confirming the formation of the hydrogel and thus allowing to begin an MRI volume follow-up study over a 14-day course. After this period, the alginate implants were carefully resected by surgery by cutting a large portion of skin and sometimes surrounding muscle when needed. Pictures were taken; one example is available in the Supporting Information section (Figure S13, Supporting Information). The remaining volumes of alginate still appeared clear and elliptical. Due to their softness and fragility, the dimensions of the hydrogel lumps were not measured with a caliper: they were directly prepared for histological fixation. However, a direct visual inspection of each sample, after each surgery, allowed to confirm that the remaining volumes of alginate expected from the MRI images (Figure 8), correlated very well in geometry and size with the volumes that were revealed at the resection step.

This MRI follow-up of the hydrogel injections was performed in parallel with a blood sampling procedure to identify potential signs of inflammation induced by the presence of the hydrogels (**Figure 7**a). The USPIONs-containing alginate hydrogels were clearly visualized on the scans throughout the duration of the study as bright regions under mice's skin (as pointed out by the white arrows in Figure 7b). The alginate hydrogels without USPIONs were visualized as dark regions well delineated by the surrounding adipose tissue.

In the first 3 days of the study, the hydrogel volume decreased most probably due to the absorption by the surrounding tissues of a large fraction of the water content, as well as by the potential release of alginate-complexing Ca^{2+} ions into the microenvironment. After 3 days, the volume almost stabilized until the

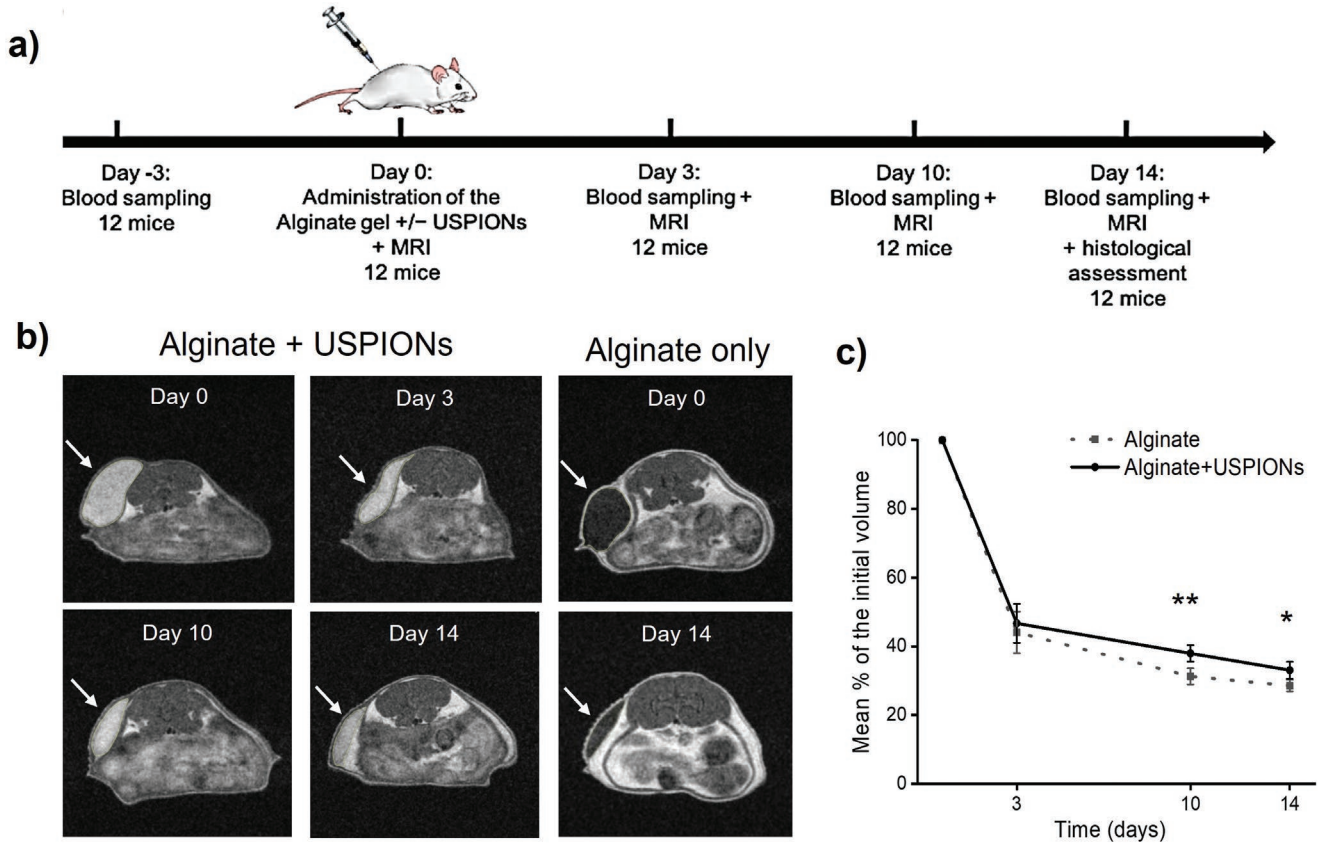

Figure 7. Volume retention study in vivo over a 14-day course. a) Timeline of the experiment. b) Representative MRI scans of mice s.c. injected with USPION-containing alginate, as well as controls (without USPIONs); the hydrogels implants are pointed with white arrows (T_1-weighted spin-echo sequence; *TR*: 480 ms, *TE*: 11 ms). c) In vivo volume retention profile of the two types of hydrogels, expressed as mean % of the initial volume and calculated from the MRI scans ($n = 6$).

end of the experiment. The profiles extracted from the MRI scans (Figure 7c) follow the same trend in both experimental groups. At day 3 post-administration, the decrease in hydrogel volume was 56% and 53% for the alginate and alginate + USPIONs groups, respectively (difference not statistically significant). On day 14 of the experiment, the residual volume of alginate injections was 28.6 ± 1.7% whereas that of the alginate + USPIONs group was 33.1 ± 2.5%. The higher volume retention noted for USPION-supplemented alginate could be explained both by the presence of PEG chains at the surface of USPIONs with which the alginate chains can interact, as well as the possible slight dissolution of iron ions at the surface of particles, which can enhance the crosslinking of alginate.

The biocompatibility of the hydrogel formulation was assessed in vivo by measuring the general inflammatory response with the cytokine test. Circulating proinflammatory (IL-6, MCP-1, IFN-γ, TNF, IL-12p70) and anti-inflammatory (IL-10) cytokines expression were measured to assess the general inflammatory response (Figure S14, Supporting Information). For mice injected with alginate only, the cytokines IL-6 and IFN-γ could not be detected as levels were all below the standard range. IL-10, MCP-1, TNF, and IL-12p70 appeared to fall within the standard range, although near the lower limit of quantitation. For the alginate + USPION group, the concentration of cytokines IL-6 and IFN-γ was again below the standard quantitation range for all time points, whereas cytokines IL-10, MCP-1, TNF, and IL-12p70 appeared close to the lower limit of quantification in the standard range. Throughout the study, the concentration of each cytokine remained around its baseline value measured on day 3. In summary, these results indicate the limited effect of alginate and alginate + USPIONs hydrogels on the general inflammatory response up to 14 days in vivo.

The local inflammatory response was also studied by immunofluorescence and hematoxylin-eosin (H&E) staining in histological preparations. Immunofluorescence and H&E images showed similar results for both experimental groups (Figure 8, as well as Figures S15 and S16, Supporting Information). The presence of hydrogel materials was clearly seen in the immunofluorescence images, and some cellular invasion (nuclear signal in blue) was observed at their surface, which suggests that, on day 14, the hydrogels had begun remodeling. A limited presence of F4/80-expressing macrophages (signal in green in the first-row images in **Figure 8**) was also found at the surface of the hydrogels and the periphery of the tissues. However, the intensity of the macrophage signal in both experimental groups (alginate and alginate + USPIONs) was very low compared to inflamed positive control tissue (Figure 8f). This suggests that only a moderate local inflammation response was developed in the tissues surrounding the implant. Representative H&E-stained images are presented in Figure 8c,d and reveal that

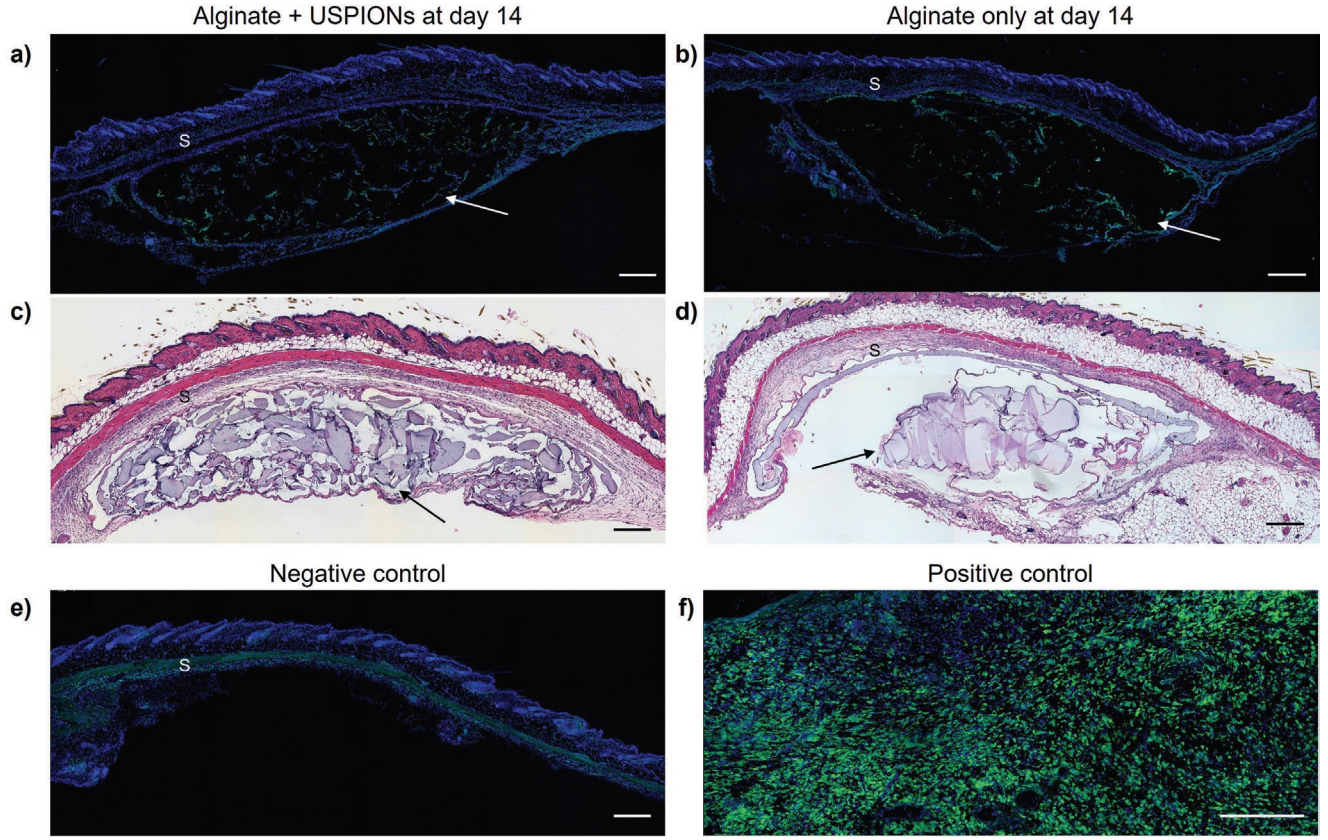

Figure 8. Histological assessment of biocompatibility following a,b) F4/80 immunostaining and Hoechst 33258 labeling and c,d) H&E staining of the alginate containing USPIONs and alginate-only hydrogels, respectively, with surrounding tissue at day 14 post-administration. e) The skin from the opposite flank of the experimental mice was used as a negative control. f) Infected murine skin was used as a positive control. Cell nuclei are stained in blue; macrophages are stained in green. The thickness of the tissue sections is 30 µm. Scale bar 500 µm. The hydrogels are pointed with arrows; the skin layer is marked with an "S."

the hydrogels were highly fragmented at day 14 post-administration. From the immunostaining results, a moderate presence of inflammatory cells was detected on the outlines of these fragments. Additional examples are shown in Figure S16, Supporting Information. Overall, these results confirm, at the microscopic and local scale, the very limited presence of macrophages in the vicinity of the implants, which agrees with the absence of circulating cytokines—and thus of general inflammation—noted in the blood tests.

2.6. Shape Fidelity Assessment of MRI-Visible Hydrogel Scaffolds by the USPION-Ink Approach Using Alginate Pore-Containing Structures

As a final step in this study, and in preparation for a future study entirely aiming at implanting alginate-USPION pore structures in vivo, sacrificial carbohydrate 3D lattice networks printed with a customized 3D printer (methodology described in the Experimental Section). Alginate pore-containing structures were thus prepared by this inverted template methodology (**Figure 9**, steps 1 and 2).[33] The 3D printing process generated self-supported filaments aligned according to orientations programed in a computer-assisted data (CAD) file (Figure 9a–c, Step 1). The resulting 3D-printed carbohydrate template had outer dimensions of $20 \times 14 \times 10$ mm^3 (Figure 9d), and the internal lattice was composed of eight alternating layers of four longitudinal and four transversal 1 mm-diameter filaments (Figure 9a–d).

As a second step, the 3D-printed carbohydrate lattices were CT-scanned for geometrical assessment and compared to the initial prints (Figure 9, step 2). The printed filaments initially programed at a diameter of 1 mm in the CAD model, had an average diameter of 1.02 ± 0.05 mm (measured by Image J on CT-scans; $n = 3$). This corroborates well the expected diameter size of the lattice from the CAD model (Figure 9, step 1). Slight shifts were evidenced in the filament spacing after careful study of the CT scans. Figure 9o is a superposition of an elevation cross-section of the CAD plan with the corresponding CT slice of the same elevation. Defects in the 3D prints are highlighted by gray/orange in the superposition image. Deviations between the printed structure and the CAD model can be attributed to viscosity effects, shrinking of the glucose/fructose ink composition, as well as to variations in the cooling rate and humidity. Overall, these results highlight the importance of perfect control over these parameters in order to reach a high fidelity in carbohydrate 3D printing. CT-scan is therefore an essential tool for the development of high-fidelity 3D shapes featuring thin and small features.

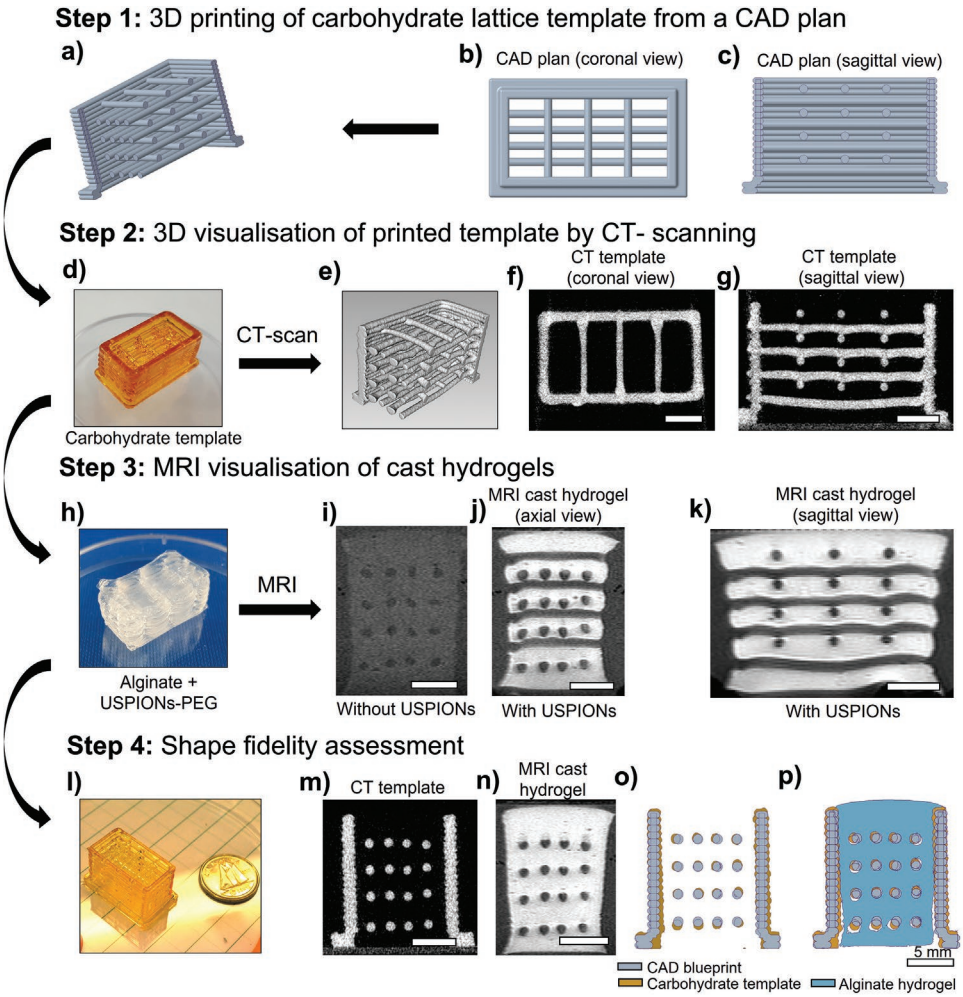

Figure 9. Four (4)-step production of MRI-visible hydrogel scaffolds by using sacrificial carbohydrate lattice templates. Step 1 (a-c): CAD blueprints of carbohydrate lattice templates. Step 2 (d-g): a freshly-printed carbohydrate lattice template ($20 \times 14 \times 10$ mm^3), and corresponding 3D reconstructed CT images (e) and cross-sections (f,g). Step 3: the freshly-molded alginate hydrogel blocs containing pore networks (h) were imaged in water using T_1-weighted MRI (i) without USPIONs; j,k) with USPIONs at 0.87 mm Fe). Step 4: from carbohydrate lattice templates (l), the CT isosurfaces were extracted (m), and were compared to the isosurfaces obtained on contrast-enhanced hydrogels in MRI (n) 0.87 mM Fe). o,p) Superposition of the carbohydrate template reconstruction from CT-scans (in orange), of the CAD models (in grey), and the isosurfaces from the MRI scanned hydrogels (in blue). Scale bar, 5 mM.

As a third step, the USPIONs-containing alginate formulation (2 wt% alginate, 0.87 mM Fe), was used to produce MRI-visible pore-containing hydrogel structures that could, in term, be implanted as cell scaffolds in vivo. This approach could be used, for instance, to enhance the capacity of blood vessels to grow and to irrigate the cells contained in the hydrogel. In this study, the molar ratio of $CaCO_3$-GDL was kept at 0.5 in order to maintain a neutral pH in the gel after complete gelation.[23] Directly after the addition of GDL to the alginate, the hydrogel was quickly mixed and carefully injected into the carbohydrate template using a syringe. The hydrogel crosslinked within 5 min and was put into a water bath to accelerate the dissolution of the carbohydrate template, leaving a highly porous hydrogel structure containing fluidic channels (Figure 9h). This type of structure will be used in future studies aiming at developing implantable adipose cell-containing scaffolds allowing more rapid vascularization.

The integrity of the interconnected channels was first demonstrated by dye perfusion in order to detect potential leaks within the channel network (Figure S17, Supporting Information). The resulting hydrogel was then visualized by MRI using a T_1-weighted spin-echo sequence (Figure 9i–k). Figure 9i,j provides a direct comparison between non-contrast-enhanced and contrast-enhanced alginate hydrogels. USPIONs-PEG produces strong positive contrast which allows to clearly visualize the channels inside the hydrogel structure (Figure 9j,k). Furthermore, the integrity of the fluidic channels can be assessed in both axial and sagittal MRI cross-sections. The average diameter of the fluidic channels was measured by ImageJ and was found to be slightly increased from 1 mm (CAD model) and 1.02 mm (CT-scans of 3D-printed carbohydrate templates) to 1.3 ± 0.1 mm in the alginate hydrogel. These results indicate that the technique can be used to mold pore networks in alginate hydrogels in a range of geometrical fidelity close to the millimeter.

Finally, images of the CAD carbohydrate template (Figure 9a–c), of the 3D-printed carbohydrate lattices obtained by CT scans (Figure 9m), as well as the MRI images of the contrast-enhanced hydrogels (Figure 9n), were superposed (see Figure 9p). The CAD template (grey) matches well the carbohydrate structure obtained by 3D-printing (orange). A fair geometrical match was found between the initial carbohydrate lattices, and the resulting channels in the hydrogel (blue). It is worth mentioning that such an isosurface match requires a high level of contrast between the hydrogel and the background, which would not be possible without the strong contrast enhancement produced by the USPIONs. Overall, the addition of USPIONs into alginate hydrogels allows a rapid and efficient assessment of geometrical fidelity between the lattice templates, and the resulting pore networks in the alginate. Enhanced contrast provided by USPIONs-PEG enables the geometric visualization of hydrogel structures with MRI, in a sub-mm resolution range, thereby revealing its fabrication defects. This strategy will be key to allowing the tracking of pore integrity and visibility in alginate cell scaffolds implanted in vivo.

3. Conclusion

In this study, USPIONs were used as a contrast agent to allow the visualization, by MRI, of alginate-based hydrogel scaffolds. The approach could find numerous applications in regenerative medicine, in particular in applications requiring follow-up with MRI, and engineered tissues transplanted in vivo. The USPIONs (TEM: ≈5 nm; DLS: ≈20 nm) used as "positive" contrast agents in T_1-weighted MRI (r_2/r_1 = 3.05, at 1 T), were stabilized by highly effective PEG-derivatized phosphine oxide ligands. Magnetometric, relaxometric, and NMRD measurements were performed on the USPIONs-PEG suspensions and USPIONs-alginate hydrogels, followed by in vitro MRI CNR measurements for a period of 30 days. The in vivo visualization of alginate scaffolds by T_1-weighted MRI was followed-up for a period of 14 days, and, in parallel, measurements by inflammatory markers and by histological analysis confirmed the biocompatibility performance of these USPION-alginate scaffolds. As a final step in this study, and in preparation for a future study entirely aiming at implanting alginate-USPION pore structures in vivo, sacrificial carbohydrate 3D lattice networks were used to fabricate alginate pore-containing structures. These structures, supplemented with USPIONs to allow MRI contrast enhancement, were used to develop a 3D-contouring procedure facilitating graft delineation and geometrical conformity assessments. This proof-of-concept with USPION-alginate preparations establishes the possibility to reveal MRI precisely engineered hydrogel structures that could be used as cell scaffolds in tissue engineering, in particular in applications requiring intensive MRI follow-ups. Overall, this study confirms the potential of USPIONs-containing biocompatible hydrogel formulations as a functional tool to delineate and follow-up cell scaffolds in regenerative medicine procedures.

4. Experimental Section

Materials Used in the Preparation of USPIONs and Hydrogel: Iron(III) chloride hexahydrate ($FeCl_3$•6 H_2O, 98%), sodium oleate (>99%), diphenyl ether (>99%), phosphorus(V) oxychloride ($POCl_3$, 99%), calcium chloride ($CaCl_2$, >93%), sodium alginate (viscosity of 15–25 cP, 1 wt% in H_2O), and GDL (>99%) were obtained from Sigma-Aldrich. Oleyl alcohol (>60%), oleic acid (>85%), and methyl ether PEG (mPEG 1000 g mol^{-1}) were obtained from TCI America. Tetrahydrofuran (THF, 99.9%), hexane (99.9%), sucrose (crystalline), and dextrose D-glucose (anhydrous) were obtained from Fisher Scientific. Calcium carbonate nanopowder ($CaCO_3$, 20–45 nm) was obtained from Skyspring. Ultrapure water (Purelab Flex 4, 18.2 MΩ.cm) was used in all experiments. Chemicals were used as-received without further purification.

Synthesis of USPIONs: USPIONs were prepared using a thermal decomposition procedure adapted from ref. [22b,34]. First, a Fe-oleate precursor was prepared by adding $FeCl_3$ (10.8 g, 40 mM), and sodium oleate (36.5 g, 120 mM) in a 250 mL round-bottom flask. A mixture consisting of EtOH (80 mL), water (60 mL), and hexane (140 mL) was added, then heated to reflux at 70 °C under vigorous agitation for 4 h. The upper organic phase was then washed three times with water using a separatory funnel, followed by hexane evaporation. A black viscous mixture was obtained, diluted in diphenyl ether to 1 g mL^{-1}, and stored at room temperature. An aliquot of this Fe-oleate solution in diphenyl ether (1.8 mL) was added to oleyl alcohol (1.897 mL, 6 mM), oleic acid (0.637 mL, 2 mM) and further diluted in diphenyl ether (8.2 mL). The resulting mixture was purged with argon for 20 min under agitation using a magnetic stirrer, followed by quick heating at 250 °C and retention at this temperature for 30 min. The solution was immediately quenched in an ice bath down to room temperature. The USPIONs were then precipitated using acetone (60 mL) followed by redispersion in hexane (10 mL). At least three washing steps were performed to purify the USPIONs prior to ligand exchange.

Ligand Exchange Procedure: The synthesis of PO-PEG was derived from a previous work by Na et al.[35] First, PO-PEG was prepared by dissolving mPEG (3 g, 3 mM) in THF (7 mL). After complete dissolution, $POCl_3$ (93 µL, 1 mM) was added prior to incubation at room temperature for 24 h. The mixture was then heated to 100 °C under a vacuum for 12 h. Finally, the product was collected and dried overnight.

PO-PEG (200 mg) dissolved in THF (3 mL), was mixed with USPIONs (100 mg), and the solvent was dried by evacuation. The mixture was heated to 150 °C under a vacuum and then incubated for 12 h. The product was cooled down to room temperature, and water (10 mL) was added to suspend the hydrophilic PEGylated USPIONs and to precipitate the residual hydrophobic ligands. Thus-suspended USPIONs were then filtrated using a 0.2 µm syringe filter and stored at 4 °C prior to further use.

Size Measurement of USPIONs-OA and USPIONs-PEG Colloids: The size of nanoparticles was measured by a TEM JEOL (JM-230) operated at 80 kV using a LaB_6 source. A small drop of the colloidal suspension was deposited on a carbon-coated copper grid (300 mesh) and allowed to dry in the air at room temperature. A size distribution profile was extracted from the TEM micrographs using ImageJ (version 1.52b; National Institutes of Health, USA).

The hydrodynamic size of the colloids was measured by DLS using a Nano Zetasizer system (Malvern Instruments, Worcestershire, UK) using a laser (He–Ne) with 633 nm wavelength and a scattering angle of 173°, at 25 °C. Oleic acid-stabilized USPIONs (USPIONs-OA) were measured in hexane (viscosity = 0.3 mPa s; refractive index (n_D) = 1.375) using a glass cuvette. PEG-stabilized USPIONs (USPIONs-PEG) were measured in water (viscosity = 0.8872 mPa s; refractive index (n_D) = 1.33) using a disposable plastic cuvette. The results of three measurements were averaged for each condition. The polydispersity index was ≈0.2–0.3 and the attenuation factor was adjusted to 8. Finally, the colloidal stability of USPIONs-PEG was measured in DLS in the following aqueous conditions: NaCl 150 mM, PBS 0.1 M, and complete DMEM (including 10% FBS and 1% penicillin). The hydrodynamic diameter was monitored at 25 °C by taking aliquots at different time points (0.5, 1, 2, 4, 6, 24, and 48 h, and then 7, 15, and 30 days).

PEGylation of the USPIONs was confirmed by FTIR spectroscopy and the number of organic ligands per nanoparticle was estimated by thermogravimetric analysis (TGA). These experiments were performed using an Agilent Cary 660 FTIR (Agilent Technologies, USA) and a TGA Q50 (TA Instruments, USA). Details about sample preparation

and analysis can be found in the Supporting Information. The iron concentration in the USPION colloids was measured using a microwave plasma atomic emission spectroscopy equipment (MP-AES 4100, Agilent) and all magnetic measurements of the colloids were carried-out on a mini high field measurement system from Cryogenics Limited (UK). More details relative to sample preparation and analysis are found in the Supporting Information.

Relaxivity Measurements and NMRD Profiling of USPIONs Colloids: The longitudinal (T_1) and transverse (T_2) relaxation times of the USPIONs-PEG colloids were measured using a time-domain NMR (TD-NMR) relaxometer (Bruker Minispec 60 mq, 60 MHz, 25 °C). An inversion-recovery (IR) sequence was used to measure T_1, whereas T_2 was extracted using a Carr–Purcell–Meibom–Gill (CPMG) sequence. The efficiency of a contrast agent was evaluated by its ability to increase the longitudinal and the transverse relaxation rates of water protons normalized to the concentration of iron (relaxivities: r_1 and r_2).[36] The measured relaxation rate ($1/T_{i,obs}$) comprised the contribution of the contrast agent ($1/T_{i,p}$), which was proportional to the iron concentration, and the diamagnetic contribution of water ($1/T_{i,d}$)

$$\frac{1}{T_{i,obs}} = \frac{1}{T_{i,d}} + \frac{1}{T_{i,p}} = \frac{1}{T_{i,d}} + [Fe]r_i \text{ where } i = 1,2 \quad (1)$$

r_1 and r_2 are respectively the longitudinal and transverse relaxivities which allowed to compare the efficiency of different contrast agents.

Thus, by calculating the slope of T_1^{-1} and T_2^{-1} plotted against the Fe concentration (determined by MP-AES), the longitudinal and transverse relaxivity values (r_1 and r_2) were obtained. Finally, the simulated signal intensity (SSI) was calculated to estimate the concentration of contrast media at which an optimal signal enhancement was expected. The SSI equation for a spin-echo sequence is described as follows[22a,37]

$$SSI = \rho\left(1 - e^{-TR/T_1}\right)\left(e^{-TE/T_2}\right) \quad (2)$$

where ρ is the proton density (ρ = 1), TR is the repetition time (TR = 400 ms), and TE is the time to echo (TE = 10.8 ms).

NMRD profiles were acquired to characterize the relaxivity behavior of USPIONs-PEG (1 mM Fe) in water and hydrogels at various magnetic field strengths. Longitudinal (r_1) NMRD profiles were measured from 0.1 to 40 MHz with a Spinmaster fast field cycling relaxometer (STELAR, Italy) and at 20, 60, 300, and 500 MHz (corresponding to 0.47, 1.41, 7, and 11.7 T; γ = 42.6 MHz/Tesla) using Bruker MiniSpec relaxometers (20 and 60 mq; 20 and 60 MHz), Avance spectrometer (300 MHz, Bruker, Germany) and Avance II spectrometer (500 MHz, Bruker, Germany). In the case of USPIONs-PEG in water, 300 µL (1 mM Fe) of USPIONs-PEG was poured into a 7 mm NMR tube. Hydrogels of 1 to 5 wt% were crosslinked directly into the NMR tube by adding 270 µL of a hydrogel, USPIONs, and $CaCO_3$ (50 mM) mixture (1 mM Fe). Hydrogel crosslinking was done by quick addition of GDL (30 µL, 1 M) followed by vigorous shaking. The hydrogel was kept at room temperature for at least 24 h before NMRD measurements. Experimental data points were corroborated with theoretical fitting provided by the relaxation mechanism of very small USPIONs described earlier by Roch et al.[29]

SEM Measurement of the Hydrogels: Morphological examination of the hydrogels (1 to 5 wt%) was performed using SEM apparatus Quanta 250 (FEI Company Inc., Thermo-Fisher Scientific). For the analysis, the hydrogels were plunged into liquid nitrogen for 10 min and lyophilized for 24 h. Samples were prepared by fixing the lyophilized hydrogel scaffolds to a holder using a conducting carbon strip and applying the gold coating. The samples were analyzed at a 15 kV electron beam.

MRI Visibility Assays of USPIONs-PEG Solutions and Hydrogel Samples: In a typical procedure, 300 µL aliquots of USPIONs-PEG were dispensed into 96-wells plates. For alginate hydrogel samples, 270 µL of an alginate solution containing $CaCO_3$ (50 mM) and USPIONs-PEG (0.96 mM Fe) was dispensed into each well and crosslinked with GDL (30 µL, 1 M). The final concentration of USPIONs-PEG was 0.87 mM. Hydrogel controls without USPIONs-PEG were prepared under the same conditions. The MRI signal generated by USPIONs-PEG colloids was measured by a 1 T small-animal MRI system (M2M, Aspect Imaging, Israel), using an RF coil for 96-well plates. The T_1-weighted spin-echo sequence used for the characterization had the following parameters: TE = 10.8 ms; TR = 400 ms; $f\alpha$ = 90°; FOV = 70 mm; 1.4 mm slices with 0.1 mm gap; dwell time = 16 µs; matrix: 200 × 200; 3 excitations. Regions of interest (ROI) were drawn over cross-sections of the tubes, and the signal intensity was integrated using the ImageJ software.

A 30-day MRI signal stability experiment was also performed. Cylindrical-shaped hydrogel objects were fabricated in 96-well plates by dispensing in each well 370 µL of a hydrogel mixture containing alginate (2%), $CaCO_3$ (50 mM), USPIONs-PEG (0.87 mM), and GDL (100 mM), which was left to react for 24 h. These hydrogels were transferred into a plastic tube containing H_2O (2.5 mL), which was imaged at 0, 0.5, 1, 2, 4, 6, 24, and 48 h and 7 days. At each time point, a T_1-weighted spin-echo sequence and a 60 mm RF coil were used as follows: TE = 15.1 ms; TR = 400 ms; $f\alpha$ = 90°; FOV = 60 mm; 1.4 mm slices with 0.1 mm gap; dwell time = 50 µs; matrix: 200 × 200; 5 excitations. ROIs were drawn over cross-sections of the samples and the signal was integrated using ImageJ. The raw signal (I_x) obtained on each sample was corrected by the control consisting of hydrogel without a contrast agent (I_{Ctl}). The signal stability over time (S_x/S_0) was assessed by comparing the mean raw signal intensity obtained on hydrogel formulations supplemented with USPIONs-PEG at t = x (S_x), incubated in water, with that of the same formulation at t = 0, expressed as follows

$$\frac{S_x}{S_0} = \frac{I_x - I_{Ctl}}{I_0 - I_{Ctl}} \quad (3)$$

The CNR was calculated using the following formula

$$CNR = \frac{I_{Hydrogel} - I_{Media}}{\sigma} \quad (4)$$

where the contrast represents the mean signal intensity of the hydrogel ($I_{Hydrogel}$) subtracted by the mean signal intensity of the surrounding media (I_{Media}), while the noise (σ) was determined by the standard deviation of the signal measured on air.

Culture of Adipose-Derived Stromal Cells: Ascorbic acid, insulin, 3,3′,5-triiodo-L-thyronine (T3), Nonidet, dexamethasone, and 3-isobutyl-1-methylxanthine (IBMX, 99%) were obtained from Sigma-Aldrich. Rosiglitazone was obtained from Cayman Chemical.

Culture of Adipose-Derived Stromal Cells and Differentiation of Adipocytes: Human adipose tissue cells were isolated using a previously described protocol,[38] under ethics protocol number 2012-1308 approved by the CRCHU-de Québec-Université Laval ethics committee. Adipose-derived stem/stromal cells (ASCs) were thawed and amplified in culture according to previous studies.[38] The expansion medium consisted of DMEM supplemented with 10% fetal calf serum (FCS) and antibiotics. For the viability assays, cells were seeded at a density of 1.5×10^5 per well ($1.56 \times 10^4/cm^2$) in 6-well plates for 48 h, in triplicates. Then, cells were incubated for 24 h with either PBS (control), alginate (1 to 3 wt%), USPIONs-PEG (1 mM Fe), or GDL (0.5 mM). Cells were thoroughly washed with PBS, then incubation was continued until confluence was almost reached 4 days post-seeding in DMEM-10% FCS. The resazurin assay was performed to assess cell viability (see details in Supporting Information).

In order to assess the maintenance of ASCs adipogenic potential, similar cultures (put in contact with the products during 24 h, 2 days after initial seeding, in triplicates) were then induced at confluency (day 7 after initial seeding) by supplementing the media with an adipogenic cocktail consisting of insulin (100 nM), 3,3′,5-triiodo-L-thyronine (T3, 0.2 nM), dexamethasone (1 mM), IBMX (0.25 mM), and 1 mM rosiglitazone (1 mM) in 3% FCS medium for 3 days, while non-induced cells were treated with 3% FCS expansion medium containing 0.038% dimethylsulfoxide (DMSO; control media), which was the diluent for IBMX and rosiglitazone. After 3 days, the induction medium was substituted by an adipocyte maintenance medium containing expansion media supplemented with insulin (100 nM), T3 (0.2 nM), and

dexamethasone (1 mM), while control-ASCs were cultured in 10% FCS expansion medium. During the entire differentiation process, media were supplemented with ascorbic acid (250 µm).

After 17 days of differentiation, ORO staining of the lipid cytoplasmic droplets was performed according to a previous protocol.[39] Briefly, cultures were rinsed, fixed with 10% buffered formalin, stained with 0.3% ORO in a mixture of isopropanol:water (3:2), and photographed (5×) with a phased contrast-microscope. The Image J software was used to calculate the surface area of the cultures covered by ORO-stained lipid-filled adipocytes.

Small-Animal Experiments and Histological Assessments of Graft Biocompatibility: For histological assessments, a 3-(*N*-morpholino) propanefulfonic acid (MOPS) solution supplemented with penicillin/gentamicin (P/G, 50 000 U mL^{-1} and 12.5 mg mL^{-1}, respectively) and fungizone (F) 0.25 mg mL^{-1} was prepared by adding 1 mL of antibiotics and fungizone to 500 mL of MOPS. Rat IgG2a F4/80 (ThermoFisher Scientific, catalog #14-4801-82) primary antibody's stock solution was prepared at a concentration of 0.5 mg mL^{-1}. Anti-rat A488 (ThermoFisher Scientific, catalog #A-21208) was used at a concentration of 0.01 mg mL^{-1}. Hoechst 33 258 nuclear marker's stock solution (Sigma Aldrich, catalog #B2883) was prepared at a concentration of 50 µg mL^{-1}. Rat isotype IgG2a antibody (Thermo Fisher Scientific, catalog #14-4321-82) was used for isotypic controls (0.1 mg mL^{-1} stock solution, 1/40 for cryosections).

Small-Animal Experiments and Histological Assessments of Graft Biocompatibility: All experiments were performed according to the guidelines of the Canadian Council on Animal Care (CCAC), and were approved by the local councils on animal care of Université Laval and the CRCHUQ-UL (approval number: 2019–140, CHU-19-031). 1 to 3-month-old healthy female Balb/c mice (Charles River, Montreal, Canada) were shaved on both flanks. Two groups of mice were used (n = 6 each): the first group was subcutaneously (s.c.) injected with 200 µL of an alginate (0.5% w/v) solution and the second group was s.c. injected with 200 µL of an alginate (0.5% w/v) solution containing 0.87 mM of USPIONs-PEG (alginate + USPIONs). At day 0, injections were performed in the right flank (under anesthesia, 2% of isoflurane, oxygen flow – 0.5 L min^{-1}) using 23 G x ¾ needles. Alginate solutions with and without USPIONs were pre-crosslinked just before the injections, as follows: 18 µL of $CaCO_3$ (0.165 M) was added to a vial containing 500 µL of the polymer solution, and vortexed for 10 s; then, 18 µL of freshly prepared GDL (0.33 M) was added, and vortexed for 10 s. These solutions were used to perform 200 µL-injections 3 min after the addition of GDL. This waiting time was found to be optimal as the polymer solution was still injectable, though jellifying quickly after the injection.

Thus-formed hydrogel implants were visualized by MRI (1 T M2M, Aspect Imaging, Netanya, Israel), immediately after injection (day 0). For this procedure, the mice were placed in a 3.5 cm diameter RF coil and scanned using a T_1-weighted 2D spin echo sequence: FOV 40 mm, 24 slices, 0.8 mm slice thickness, 0.1 mm slice gap, dwell time 16 µs, 280 × 280, $f\alpha$ 90°, TE/TR: 11/480 ms, 6 excitations, duration: 13 min. Scanning was repeated on days 3, 10, and 14. The MR-images were then analyzed by the OsiriX Lite software (Pixmeo SARL, Switzerland). ROIs were drawn on each MR slice, over the areas corresponding to the presence of the hydrogel grafts. Hydrogel's volumes were then computed automatically, and volume retention profiles were generated.

At the end of the follow-up study, the hydrogel implants were removed by surgical resection. Because alginate gels are very soft and fragile, complete tissue volumes including the surrounding skin and muscle—the surrounding tissue—were extracted using a surgical kit. The hydrogel volumes were photographed, prior to their histological preparation without further dissection. The skin from the opposite flank was used as a negative control for labeling. Inflamed skin of CD-1 mice was used as a positive control for macrophage labeling. All incubations for histological preparations were carried out at room temperature unless specified otherwise. The tissues were fixed in a 3.7% formalin-MOPS solution using histological cassettes. They were incubated for 1–2 h, then transferred in a 1% MOPS-BSA solution, incubated for 1.5 h, and sliced with a surgical scalpel (#4, blade #22) as shown in Figure S13, Supporting Information. The tissues were then processed in two different ways: inclusion in paraffin for H&E staining and inclusion in optimal cutting temperature (OCT) compound for immunofluorescence staining.[40] Details about the two processes can be found in the Supporting Information. Images were acquired with an LSM 700 confocal microscope and the Zen 2010 software (Zeiss).

Development of a Sacrificial Carbohydrate Template for the Production of a Pore Network: The level of precision of volume and contours rendering by MRI and using the addition of USPIONs to the hydrogel was assessed with blocks of hydrogel containing oriented pore structures. These pore structures in hydrogel volumes were generated by an inverted template approach. First, sacrificial carbohydrate 3D lattice networks were printed with a customized 3D printer.[33] Sucrose (62.4 g, 0.182 mol) and glucose (15.6 g, 0.087 mol) were dissolved in demineralized water (50 mL). This mixture was heated to 175 °C, which removed most of the water and produced a viscous solution. Meanwhile, a second mixture was prepared by dissolving sucrose (5 g, 15 mM), glucose (1.2 g, 7 mM), and calcium chloride (0.3 g, 3 mM) into demineralized water (8 mL). The solution was heated to 140 °C, while the first mixture was maintained above 130 °C. Then, using a spatula, the two solutions were carefully mixed for 1 min while avoiding air bubbles in the mix, followed by transfer into 20 mL glass syringes, preheated at 120 °C. The glass syringes were loaded on a custom 3D printer. A carbohydrate glass frame with inner dimensions of 20 × 10 × 14 mm, containing eight alternating layers of four longitudinal and three transversal 1 mm-diameter inner filaments (to generate pore structures) was printed (Figure 1b). During the printing, the temperatures of the glass syringe and the extrusion nozzle were respectively maintained at 115 and 95 °C, and the self-supported filaments were cooled with air nozzles. The printer was operated using G-code commands, managed by the Repetier–Host software (version 2.1.3), and programmed manually. An Arduino Mega2560 micro-controller was used to interpret commands and execute proper actions on the printer, using the open-source Marlin firmware (version 1.1.9). The 3D-printed carbohydrate lattices were CT-scanned for geometrical assessment and comparison with the initial prints (GE Locus 80 CT scanner; voltage = 40 kV; current = 100 µA; exposure time = 100 ms; detector binning of 4 × 4 for a voxel resolution = 89 µm). Image reconstruction was performed using the Parallax Innovations (Canada) Reconstruction Tool Software.

Molding of MRI-Visible Hydrogel Scaffolds with Pore Networks: A USPIONs-containing alginate precursor solution was prepared by mixing sodium alginate in water (9 mL, 2.22 wt%) with USPIONs, $CaCO_3$ (50 mM), and freshly prepared GDL solution (1 mL; 1 M), thus yielding a 2 wt% alginate-USPIONs with 0.87 mM Fe (optimal contrast-enhancement concentration—see relaxivity section in the Supporting Information). The $CaCO_3$:GDL molar ratio was kept to 0.5 in order to maintain a neutral pH in the gel after complete gelation.[9b] The hydrogel was quickly mixed and injected onto the carbohydrate lattice, and left for crosslinking for 5 min. Then it was put into a water bath to fully dissolve sugar and remove the excess carbohydrates. The resulting hydrogel was stored at 4 °C prior to imaging.

MR-Imaging of Hydrogel Scaffolds, Image Processing, and Analysis: The scaffolds were then MR-imaged. They were fixed with a plastic sample holder filled with nanopure water and control hydrogels (i.e., with and without USPIONs-PEG). A 35 mm RF coil and T_1-weighted spin-echo sequence were used as follows: TE = 23.1 ms; TR = 400 ms; $f\alpha$ = 90°; FOV = 40 mm; 0.9 mm slices with 0.1 mm gap; dwell time = 50 µs; matrix: 352 × 200; 15 exc.

Finally, the CT images from the carbohydrate templates, and the MRI images from the resulting hydrogel scaffolds, were converted into standard tessellation language (STL) files to allow comparative analyses. STL files from the sacrificial carbohydrate lattice network templates were generated directly from the CT-scan data on MicroView from Parallax Innovations (Canada), whereas that of the hydrogel structures obtained by MRI were first converted into a Digital Imaging and Communications in Medicine (DICOM) file using the NRGSYS software (Aspect Imaging, Israel) followed by their conversion into STL files using the OsiriX

software from Pixmeo SÀRL (Switzerland). Finally, image superposition for geometrical fidelity and MRI volume rendering assessment was performed on the CREO Parametric software version 4.0 M030 (USA) and aligned manually.

Statistical Analysis: Unless otherwise stated, all experimental results were expressed as mean ± SD. Statistical analysis was performed using the one-way ANOVA (GraphPad Prism 8.0 Software). The results were considered statistically significant for $p < 0.05$. For animal experiments, the statistical differences between the control and experimental groups were analyzed according to the paired Student's *t*-test. Statistical significances were presented when the *p*-value was less than 0.05 (*) and less than 0.005 (**).

Supporting Information

Supporting Information is available from the Wiley Online Library or from the author.

Acknowledgements

This research was supported by the Natural Science and Engineering Research Council (NSERC) of Canada (Discovery Grant RGPIN-2017-06173); and the Polymer Nanoparticles for Drug Delivery (PoND) Training Program (NSERC-CREATE 497311; M.-A.F.). M.-A.F. and S.L. are grateful to the Ministère des Relations internationales du Québec and to the Wallonnie-Bruxelles Region for a collaborative grant (Project 2017–2019 – 10.803). The confocal imaging system was obtained through the Fonds des Leaders program from the Canada Foundation for Innovation (CFI) to J.F. M.-A.F. is a member of the Centre Québécois sur les Matériaux Fonctionnels (CQMF). The authors acknowledge the valuable contributions of Dr. Pascale Chevallier (physicochemical characterization and manuscript revision), Dr. Jean Lagueux (MRI), Mrs. Gabrielle Gauvin-Rossignol (carbohydrate 3D-printing), Mrs. Vicky Dodier (MP-AES), Mr. Richard Janvier (TEM), Mr. Christopher Bérubé (^{31}P NMR), and Dr. Cindy J. Hayward (cell culture). MRI studies were performed at the small animal imaging platform (CHU de Québec – Université Laval Research Center) with the help of Dr. Jenny Roy and T.L. The authors acknowledge the flow cytometry core facility of the CHU de Quebec Research Center for their help in providing data for this publication, especially Dr. Éric Boilard, Isabelle Allaeys, and Etienne Doré.

Conflict of Interest

The authors declare no conflict of interest.

Author Contributions

S.L.-C. and M.K. contributed equally to this work. The manuscript was written through the contributions of all authors. The experiments were mainly designed by M.-A.F. and performed by M.K., S.L., and P.L. The manuscript was mainly written by M.A.-F. with M.K., S.L. (nanoparticles preparation and physicochemical characterization, MRI imaging, hydrogel preparation, and characterization), and P.L. (hydrogel and nanoparticles preparations) as main contributors to the texts. C.H., S.L., and Y.G. designed and performed magnetic and NMRD measurements and analyses; J.F. and her team designed and performed cell culture experiments and related analyses, as well as worked on the alginate graft preparation procedures and interpretation of results (D.M.); S.C., P.L., J.R., and A.B.-D. designed and performed experiments related to the fabrication of the inverted sugar templates. All authors have given approval for the final version of the manuscript.

Data Availability Statement

The data that support the findings of this study are available from the corresponding author upon reasonable request.

Keywords

alginate hydrogel scaffolds, cell scaffolds, soft tissue imaging, T_1-weighted magnetic resonance imaging (MRI), tissue engineering, ultra-small iron oxide nanoparticles, contrast agents

Received: October 27, 2022
Revised: December 29, 2022
Published online:

[1] a) G. D. Nicodemus, S. J. Bryant, *Tissue Eng.* **2008**, *14*, 149; b) S. V. Murphy, A. Atala, *Nat. Biotechnol.* **2014**, *32*, 773; c) E. Caló, V. V. Khutoryanskiy, *Eur. Polym. J.* **2015**, *65*, 252; d) J. L. Drury, D. J. Mooney, *Biomaterials* **2003**, *24*, 4337; e) S. Van Vlierberghe, P. Dubruel, E. Schacht, *Biomacromolecules* **2011**, *12*, 1387; f) H. Tan, K. G. Marra, *Materials* **2010**, *3*, 1746.

[2] K. M. Bratlie, R. L. York, M. A. Invernale, R. Langer, D. G. Anderson, *Adv. Healthcare Mater.* **2012**, *1*, 267.

[3] a) M. Hamidi, A. Azadi, P. Rafiei, *Adv. Drug Delivery Rev.* **2008**, *60*, 1638; b) G. W. Ashley, J. Henise, R. Reid, D. V. Santi, *Proc. Natl. Acad. Sci. USA* **2013**, *110*, 2318; c) J. Li, D. J. Mooney, *Nat. Rev. Mater.* **2016**, *1*, 16071.

[4] a) N. A. Peppas, J. J. Sahlin, *Biomaterials* **1996**, *17*, 1553; b) M. Kiseleva, M. M. Omar, É. Boisselier, S. V. Selivanova, M.-A. Fortin, *ACS Biomater. Sci. Eng.* **2022**, *8*, 1200.

[5] a) J. A. Hunt, R. Chen, T. van Veen, N. Bryan, *J. Mater. Chem. B* **2014**, *2*, 5319; b) B. Guillotin, F. Guillemot, *Trends Biotechnol.* **2011**, *29*, 183; c) M. Santoro, J. Navarro, J. P. Fisher, *Small Methods* **2018**, *2*, 1700318.

[6] A. K. Gaharwar, N. A. Peppas, A. Khademhosseini, *Biotechnol. Bioeng.* **2014**, *111*, 441.

[7] a) F. Pati, J. Jang, D.-H. Ha, S. W. Kim, J.-W. Rhie, J.-H. Shim, D.-H. Kim, D.-W. Cho, *Nat. Commun.* **2014**, *5*, 3935; b) K. Y. Lee, D. J. Mooney, *Chem. Rev.* **2001**, *101*, 1869.

[8] J. Malda, J. Visser, F. Melchels, T. Jüngst, W. Hennink, W. Dhert, J. Groll, D. Hutmacher, *Adv. Mater.* **2013**, *25*, 5011.

[9] a) J. Jia, D. J. Richards, S. Pollard, Y. Tan, J. Rodriguez, R. P. Visconti, T. C. Trusk, M. J. Yost, H. Yao, R. R. Markwald, Y. Mei, *Acta Biomater.* **2014**, *10*, 4323; b) C. K. Kuo, P. X. Ma, *Biomaterials* **2001**, *22*, 511; c) K. Y. Lee, D. J. Mooney, *Prog. Polym. Sci.* **2012**, *37*, 106.

[10] a) M. Chen, G. Gong, L. Zhou, F. Zhang, *RSC Adv.* **2017**, *7*, 21476; b) N. Annabi, A. Tamayol, J. A. Uquillas, M. Akbari, L. E. Bertassoni, C. Cha, G. Camci-Unal, M. R. Dokmeci, N. A. Peppas, A. Khademhosseini, *Adv. Mater.* **2014**, *26*, 85; c) K. J. De France, F. Xu, T. Hoare, *Adv. Healthcare Mater.* **2018**, *7*, 1700927.

[11] a) M. Hospodiuk, M. Dey, D. Sosnoski, I. T. Ozbolat, *Biotechnol. Adv.* **2017**, *35*, 217; b) D. Chimene, K. K. Lennox, R. R. Kaunas, A. K. Gaharwar, *Ann. Biomed. Eng.* **2016**, *44*, 2090.

[12] P. Sikorski, F. Mo, G. Skjåk-Bræk, B. T. Stokke, *Biomacromolecules* **2007**, *8*, 2098.

[13] a) Y. Dong, G. Jin, C. Ji, R. He, M. Lin, X. Zhao, A. Li, T. Jian Lu, F. Xu, *Acta Biomater.* **2017**, *55*, 410; b) A. Berdichevski, H. Simaan Yameen, H. Dafni, M. Neeman, D. Seliktar, *Proc. Natl. Acad. Sci. USA* **2015**, *112*, 5147.

[14] K. Lei, Q. Ma, L. Yu, J. Ding, *J. Mater. Chem. B* **2016**, *4*, 7793.

[15] N. T. Thanh, *Clinical Applications of Magnetic Nanoparticles: From Fabrication to Clinical Applications*, CRC Press, Boca Raton, FL **2018**.
[16] a) T. Courant, V. G. Roullin, C. Cadiou, M. Callewaert, M. C. Andry, C. Portefaix, C. Hoeffel, M. C. de Goltstein, M. Port, S. Laurent, L. V. Elst, R. Muller, M. Molinari, F. Chuburu, *Angew. Chem., Int. Ed.* **2012**, *51*, 9119; b) J. Liu, K. Wang, J. Luan, Z. Wen, L. Wang, Z. Liu, G. Wu, R. Zhuo, *J. Mater. Chem. B* **2016**, *4*, 1343; c) S. Sarkis, F. Silencieux, K. E. Markwick, M.-A. Fortin, C. A. Hoesli, *ACS Biomater. Sci. Eng.* **2017**, *3*, 3576; d) A. J. Shuhendler, R. Staruch, W. Oakden, C. R. Gordijo, A. M. Rauth, G. J. Stanisz, R. Chopra, X. Y. Wu, *J. Controlled Release* **2012**, *157*, 478.
[17] R. Chen, D. Ling, L. Zhao, S. Wang, Y. Liu, R. Bai, S. Baik, Y. Zhao, C. Chen, T. Hyeon, *ACS Nano* **2015**, *9*, 12425.
[18] a) M. Killer, E. M. Keeley, G. M. Cruise, A. Schmitt, M. R. McCoy, *Neuroradiology* **2011**, *53*, 449; b) Z. Chen, C. Yan, S. Yan, Q. Liu, M. Hou, Y. Xu, R. Guo, *Theranostics* **2018**, *8*, 1146; c) F. Shen, C. Poncet-Legrand, S. Somers, A. Slade, C. Yip, A. M. Duft, F. M. Winnik, P. L. Chang, *Biotechnol. Bioeng.* **2003**, *83*, 282.
[19] a) R. Qiao, C. Yang, M. Gao, *J. Mater. Chem.* **2009**, *19*, 6274; b) Z. Gao, T. Ma, E. Zhao, D. Docter, W. Yang, R. H. Stauber, M. Gao, *Small* **2016**, *12*, 556.
[20] Y. Lu, Y.-J. Xu, G.-b. Zhang, D. Ling, M.-q. Wang, Y. Zhou, Y.-D. Wu, T. Wu, M. J. Hackett, B. Hyo Kim, H. Chang, J. Kim, X.-T. Hu, L. Dong, N. Lee, F. Li, J.-C. He, L. Zhang, H.-Q. Wen, B. Yang, S. Hong Choi, T. Hyeon, D.-H. Zou, *Nat. Biomed. Eng.* **2017**, *1*, 637.
[21] Z. Shen, A. Wu, X. Chen, *Mol. Pharmaceutics* **2017**, *14*, 1352.
[22] a) W. Xiao, P. Legros, P. Chevallier, J. Lagueux, J. K. Oh, M.-A. Fortin, *ACS Appl. Nano Mater.* **2018**, *1*, 894; b) B. H. Kim, N. Lee, H. Kim, K. An, Y. I. Park, Y. Choi, K. Shin, Y. Lee, S. G. Kwon, H. B. Na, J.-G. Park, T.-Y. Ahn, Y.-W. Kim, W. K. Moon, S. H. Choi, T. Hyeon, *J. Am. Chem. Soc.* **2011**, *133*, 12624; c) H. J. Kwon, K. Shin, M. Soh, H. Chang, J. Kim, J. Lee, G. Ko, B. H. Kim, D. Kim, T. Hyeon, *Adv. Mater.* **2018**, *30*, 1704290; d) P. Li, W. Xiao, P. Chevallier, D. Biswas, X. Ottenwaelder, M.-A. Fortin, J. K. Oh, *ChemistrySelect* **2016**, *1*, 4087; e) N. Chan, M. Laprise-Pelletier, P. Chevallier, A. Bianchi, M.-A. Fortin, J. K. Oh, *Biomacromolecules* **2014**, *15*, 2146; f) H. Wei, O. T. Bruns, M. G. Kaul, E. C. Hansen, M. Barch, A. Wiśniowska, O. Chen, Y. Chen, N. Li, S. Okada, J. M. Cordero, M. Heine, C. T. Farrar, D. M. Montana, G. Adam, H. Ittrich, A. Jasanoff, P. Nielsen, M. G. Bawendi, *Proc. Natl. Acad. Sci. USA* **2017**, *114*, 2325; g) N. Lee, D. Yoo, D. Ling, M. H. Cho, T. Hyeon, J. Cheon, *Chem. Rev.* **2015**, *115*, 10637.
[23] Y. Gossuin, P. Gillis, A. Hocq, Q. L. Vuong, A. Roch, *Wiley Interdiscip. Rev.: Nanomed. Nanobiotechnol.* **2009**, *1*, 299.
[24] a) U. I. Tromsdorf, O. T. Bruns, S. C. Salmen, U. Beisiegel, H. Weller, *Nano Lett.* **2009**, *9*, 4434; b) J. Zeng, L. Jing, Y. Hou, M. Jiao, R. Qiao, Q. Jia, C. Liu, F. Fang, H. Lei, M. Gao, *Adv. Mater.* **2014**, *26*, 2694; c) L. E. W. LaConte, N. Nitin, O. Zurkiya, D. Caruntu, C. J. O'Connor, X. Hu, G. Bao, *J. Magn. Reson. Imaging* **2007**, *26*, 1634.
[25] S. Laurent, D. Forge, M. Port, A. Roch, C. Robic, L. Vander Elst, R. N. Muller, *Chem. Rev.* **2008**, *108*, 2064.
[26] N. Chan, P. Li, J. K. Oh, *ChemPlusChem* **2014**, *79*, 1342.
[27] J. Y. Park, P. Daksha, G. H. Lee, S. Woo, Y. Chang, *Nanotechnology* **2008**, *19*, 365603.
[28] G. H. Simon, J. von Vopelius-Feldt, Y. Fu, J. Schlegel, G. Pinotek, M. F. Wendland, M.-H. Chen, H. E. Daldrup-Link, *Invest. Radiol.* **2006**, *41*, 45.
[29] A. Roch, R. N. Muller, P. Gillis, *J. Chem. Phys.* **1999**, *110*, 5403.
[30] R. P. Friedrich, I. Cicha, C. Alexiou, *Nanomaterials* **2021**, *11*, 2337.
[31] A. Ohki, S. Saito, K. Fukuchi, *Sci. Rep.* **2020**, *10*, 13684.
[32] M. Proulx, K. Aubin, J. Lagueux, P. Audet, M. Auger, M. A. Fortin, J. Fradette, *Tissue Eng., Part C* **2015**, *21*, 693.
[33] A. Bégin-Drolet, M.-A. Dussault, S. A. Fernandez, J. Larose-Dutil, R. L. Leask, C. A. Hoesli, J. Ruel, *Addit. Manuf.* **2017**, *15*, 29.
[34] J. Park, K. An, Y. Hwang, J.-G. Park, H.-J. Noh, J.-Y. Kim, J.-H. Park, N.-M. Hwang, T. Hyeon, *Nat. Mater.* **2004**, *3*, 891.
[35] H. B. Na, I. S. Lee, H. Seo, Y. I. Park, J. H. Lee, S.-W. Kim, T. Hyeon, *Chem. Commun.* **2007**, *48*, 5167.
[36] L. Faucher, Y. Gossuin, A. Hocq, M.-A. Fortin, *Nanotechnology* **2011**, *22*, 295103.
[37] L. Faucher, A.-A. Guay-Bégin, J. Lagueux, M.-F. Côté, É. Petitclerc, M.-A. Fortin, *Contrast Media Mol. Imaging* **2011**, *6*, 209.
[38] M. Vermette, V. Trottier, V. Ménard, L. Saint-Pierre, A. Roy, J. Fradette, *Biomaterials* **2007**, *28*, 2850.
[39] M. Vallée, J. F. Côté, J. Fradette, *Pathol. Biol.* **2009**, *57*, 309.
[40] D. Mayrand, J. Fradette, in *Adipose-Derived Stem Cells: Methods and Protocols*, (Eds: B. A. Bunnell, J. M. Gimble), Springer, New York **2018**, pp. 93–105.